microwave JOURNAL

contents

VOLUME 25, NUMBER 12
USPS 396-250
DECEMBER 1982

ON THE COVER: The continuous extension of solid-state amplifier technology is typified by the multi-octave 1 watt unit pictured. Photo: Akis Photography, New York, NY courtesy of Mini Circuits.

Press run for this issue is 45,558 copies.

EXECUTIVE EDITORIAL OFFICE
610 Washington Street, Dedham, MA 02026
Tel: 617 326-8220 710 348-0481
TELEX: 951-659
MICROSOL DEDM

EUROPEAN EDITORIAL OFFICE
25 Victoria Street London SW1H OEH England
Tel: 01-222-0466 **TELEX:** 885744

Microwave Journal is issued without charge upon written request to qualified persons working in that portion of the electronics industry including governmental and university installation that deal with VHF through light frequencies. Other subscriptions; domestic, $36 per year, two year subscriptions $65; foreign, $48 per year, two year subscriptions $85: back issues (if available) and single copies $5.00.

POSTMASTER: send address corrections to Microwave Journal, 610 Washington Street, Dedham MA 02026.

BPA

Horizon House also publishes Telecommunications and Journal of Electronic Defense

Beam Forming Networks Using Composite Phase Shifters

Marshall J. Maple,
Robert B. Wilds,
J. Keith Hunton
GTE Systems

Introduction

This paper describes an innovative beam forming network (BFN) design which uses all-pass networks in conjuction with bandpass networks to provide very low phase ripple. The networks were developed at GTE Sylvania Western Division as part of an angle of arrival (AoA) system which has AoA capability from 0.5 GHz to 8 GHz and sum pattern capability from 0.5 GHz to 18 GHz. The microwave portion of the AoA system consists of three major subsystems blocks: the antenna feed, frequency multiplexers, and the BFN. A six element monopulse antenna serves as the broadband feed. The signals from the broadband feed are then multiplexed into six frequency bands: 0.5-0.85, 0.85-2.0, 2.0-4.0, 4.0-8.0, 8.0-12.0, and 12.0-18.0 GHz by means of phase matched multiplexers. The multiplexers are state-of-the-art devices employing common junction triplexers rather than a cascade of lowpass and highpass filters. The BFN, the subject of this paper, is made up of four basic components, 4.77 dB couplers, 3.01 dB couplers, phase shift networks, and their accompanying reference networks. There are six BFN's, one for each multiplexed band. Components for the BFN's for the upper five frequency bands were developed in-house and this development is described below.

The BFN

The BFN is made of two functional blocks; a 60 degree network, and a 180 degree network. The 60 degree network is required for the generation of phase angles which are other than multiples of 90 degrees. A 60 degree phase progression for excitation at ports 1 through 6 is realized by the addition of two quadrature vectors having unequal magnitudes. This addition is accomplished by two 3.01 dB couplers and a single 4.77 dB coupler, as shown in the lower portion of Figure 1.

Table 1 shows the desired relationships between the input ports 1-6 when the BFN is fed from the sum and difference ports. The paths from element 1 to $\Sigma 1$ is the reference path for the BFN. All angles are positive. The discrete

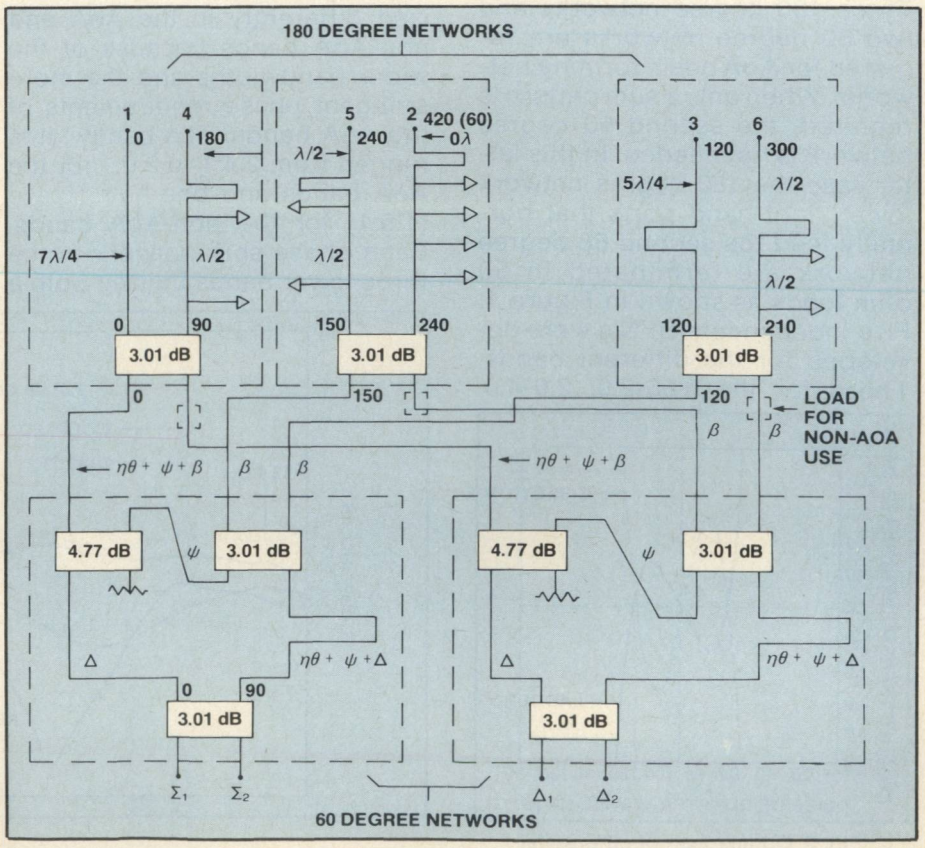

Fig. 1 BFN block diagram.

line lenths, Δ, ψ, β, and $n\theta$ are required to maintain the proper phase and amplitude relationships throughout the BFN. The length $n\theta$ is the length of the coupler sections, $\lambda/4$ for a single section coupler. In Figure 1 the relative phases of signals paths from $\Sigma 1$ to elements 1 through 6 are shown at different points in the BFN. The phases shown are relative, all paths being referenced to path $\Sigma 1$ to element 1. Within the 180 degree network, line lengths between the $\lambda/4$ stubs are $\lambda/4$ unless otherwise noted. For line lengths not assigned a length, assume zero line length.

The 180 degree network consists of a 90 degree differential phase shift network cascaded with a 90 degree 3.01 dB hybrid. The 180 degree networks are characterized by the fact that for two signals fed into port pairs 1 and 4, 2 and 5, 3 and 6, the difference of the two signals appears at the left-hand lower port and the sum of the two at the right-hand lower port. There are three versions of the 180 degree network, each consisting of a differential phase shift network and a 3.01 dB hybrid. Three 180 degree networks and two 60 degree networks are required for AoA beam forming networks. When only a sum pattern is required, the second 60 degree network is not needed. In this latter case the 180 degree network lower right-hand ports that normally feed the second 60 degree network are terminated in 50 ohm loads as shown in Figure 1. Five independent BFN's were developed for the different bands. Those for the 0.85-2.0, 2.0-4.0, and 4.0-8.0 GHz bands have the configuration of Figure 1. For the 8.0-12.0 and 12.0-18.0 GHz bands the lower right-hand ports of the 180 degree networks are terminated.

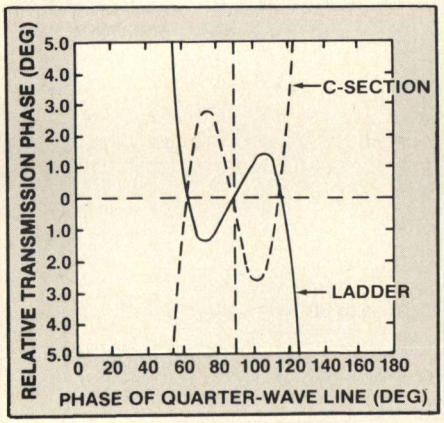

Fig. 2 Comparison of differential phase error.

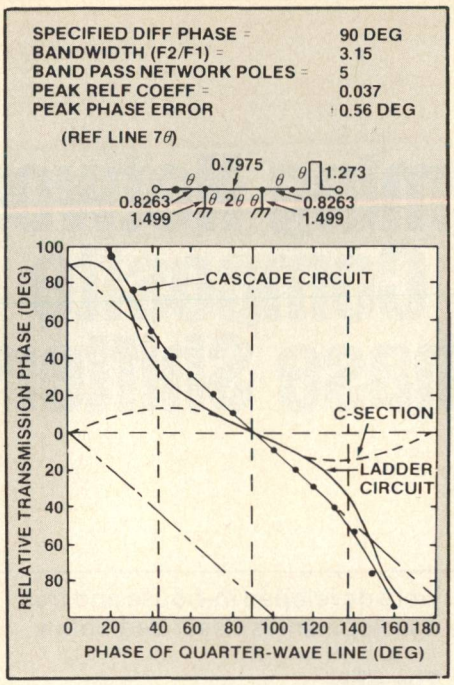

Fig. 3 Response of "C" section, ladder section & cascade.

The phase shifters used in the 180 degree networks were realized differently in the AoA and non-AoA bands because of the wider bandwidths and the more stringent phase requirements of the AoA bands. The bandwidths ranged from 2.4:1 to 2.0:1 for the AoA bands and one-half octave (1.5:1) for the non-AoA bands. Each phase shift network in the three lower bands utilized both a Shiffman C-section and a ladder network in cascade[1]. The phase ripple (error) from nominal offset of the ladder network, when compared to a reference line, has the opposite sign when compared with the phase ripple of a C-section, as shown in Figure 2. Therefore, the resulting phase deviation from nominal offset for the composite network can be made lower than in the case for C-sections of comparable complexity when used alone. For example, in Figure 3 is shown the calculated phase reponse of a cascaded phase shifter for a bandwidth of 3.15:1 from the above referenced article. The maximum phase error over the band is $\pm 0.6°$.

Actual hardware was developed to operate over a range of bandwidths, the largest being 2.4:1, and the smallest, 1.5:1. In the wider bandwidths both airline and stripline versions of the phase shifters were constructed and a phase error on the order of ± 1.0 degree was obtained. For the smaller bandwidth (1.5:1), the phase shifters were realized by a ladder structure alone. The phase shifters are then connected to the mutually isolated ports of a directional coupler. Therefore, by using the quadrature properties of the coupler, 90 degrees between the coupled and direct ports, the 90 degrees net phase shift of the phase shift network, a 180 degree phase shift is realized. Phase slope was designed into some of the phase shifters to compensate for differences in the signal paths.

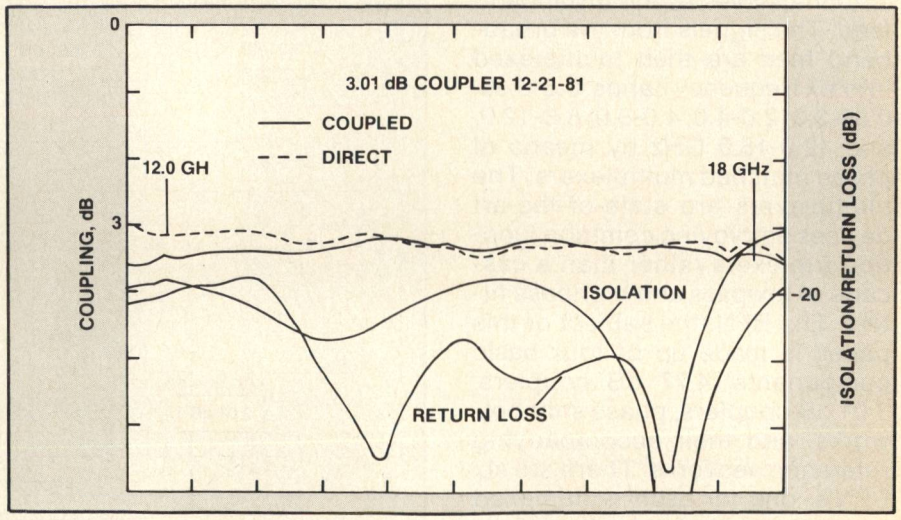

Fig. 4 Response of 3.01 dB 12-18 GHz stripline coupler.

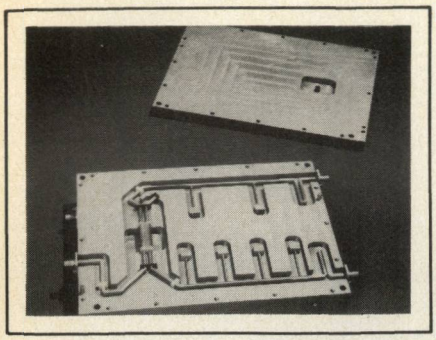

Fig. 5 2-4 GHz 180-degree network, ports 2 & 5.

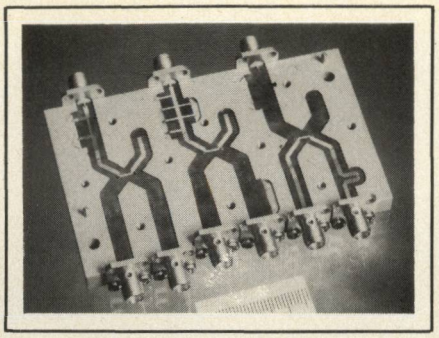

Fig. 7 12-18 GHz 180-degree networks, stripline.

This difference is due to the total number of couplers in each of the paths. The couplers exhibit a dispersive phase response.

At the lower end of the frequency band the insertion phase exceeds that of an equivalent transmission line and the opposite occurs at the high end. The amount of dispersion is inversely proportional to the bandwidth. Therefore, the amount of compensation depends upon the frequency band. Two different types of couplers were developed for the BFN: re-entrant, and offset designs. A re-entrant design was developed in both airline (from 2-4 and 4-8 GHz) and stripline (from 0.85-2 GHz). An airline re-entrant coupler was built for use above 8 GHz, however, the smaller physical size and tolerances of the parts required for acceptable performance were impractical. Instead, over/under offset couplers were developed in stripline for use from 8-12 GHz and 12-18 GHz.

During the design and development of the individual components for the BFN, special effort was made to achieve return losses greater than 20 dB. Thus, when the complete BFN was assembled with its many interconnections, the interaction of the VSWR's would be acceptable. This goal was generally reached, with a few exceptions in the 12 to 18 GHz band. Figure 4 is a plot of 3.01 dB stripline coupler response. The 2-4 GHz and 4-8 GHz units employed airline construction along with limited component integration to form "super-components" for the separate 60 degree and 180 degree networks. Airline was preferred in these bands to minimize insertion loss. The Shiffman C-sections, along with the connecting lines between components were of square cross-section. These sections and lines were fabricated using precision electron-discharge machining techniques which are capable of holding very tight tolerances on complicatd line configurations. Photos of the 2-4 GHz units are shown in Figures 5 and 6.

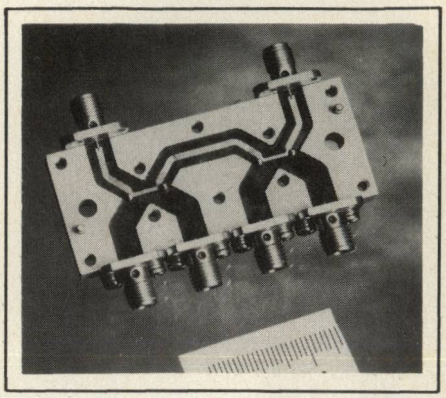

Fig. 8 8-12 GHz 4.77 dB and 3.01 dB couplers.

Virtually the same sort of integration was used in the 8-12 GHz and 12-18 GHz bands, using stripline rather than airline construction. Some of the 12-18 GHz components are shown in Figures 6 and 7. The 0.85 to 2.0 GHz band presented a less severe VSWR problem, therefore separate components were used throughout. A stripline realization was used here rather than airline because of physical size. Interconnections between components and super-components were made with 0.141" diameter semi-rigid cables, which required phase matching. A principle objective on future BFN development would be more extensive component integration.

In order to test or phase match any of these components with sufficient accuracy, a computer-controlled network analyzer with error correction was procured from Hewlett-Packard. The computer correction process involves an elaborate calibration procedure to mathematically eliminate the effect of connectors on a given component and provide, in effect, measurements of the device itself. Appropriate software modifications allowed the improvement of the phase measurement accuracy to ± 0.1 degree and also allow the measurement of one component normalized to another. Additionally, considerable software has been developed to allow the opti-

[Continued on page 84]

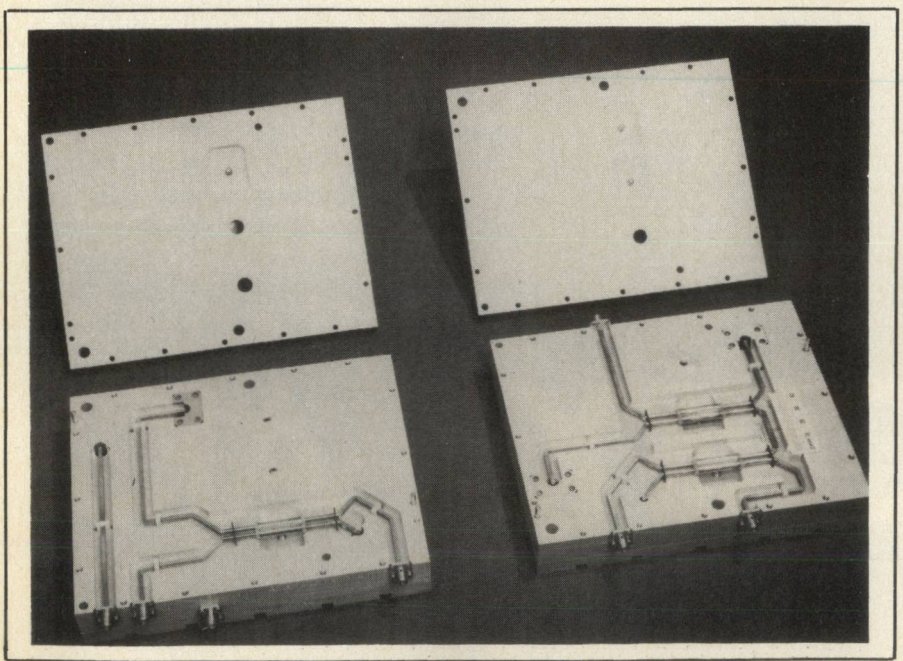

Fig. 6 2-4 GHz 60-degree network, top and bottom views.

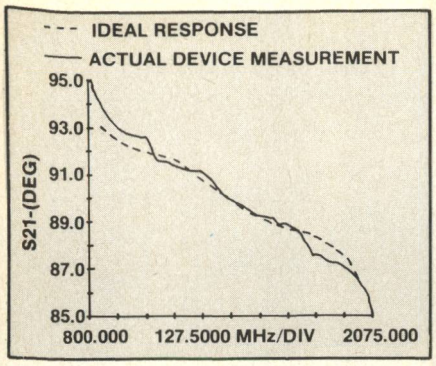

Fig. 9 Response of "C" section & ladder section cascade for port 5, stripline.

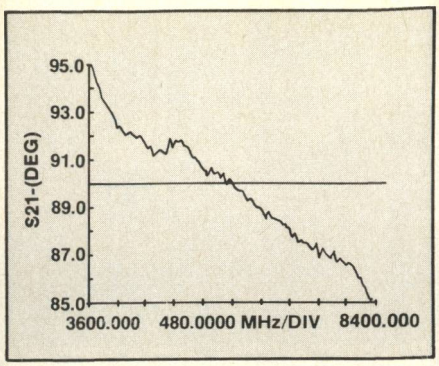

Fig. 10 Response of "C" section & ladder section cascade for port 5, airline.

mization of any BFN component, thereby allowing initial component designs which are near optimum.

A sample of some of the final data taken on various components is shown in Figures 4 through 12. Figure 9 shows the measured response of a complete ladder and C-section pair for the 0.85 to 2 GHz frequency band, and also the ideal curve which was generated by a computer program. The phase shifter was designed to be centered at 90 degrees and have an offset of 2.75 degrees for compensation of the coupler reponse. Figure 10 is the integrated response of Figures 11 and 12, which

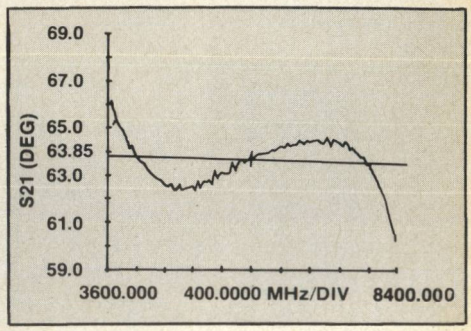

Fig. 11 Port 5 ladder section response, airline.

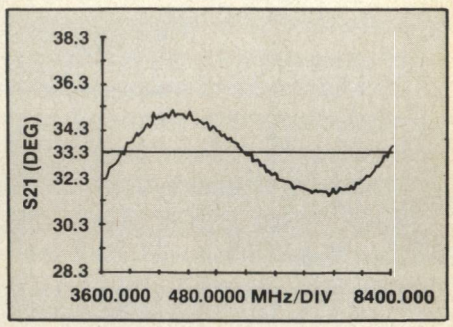

Fig. 12 Port 5 "C" section response, airline.

are, respectively, of the ladder and the C-section designed for the 4-8 GHz band. This phase network was realized in airline, whereas the phase shift network, whose response is shown in Figure 9, is in stripline.

BFN Test Results — Amplitude Measurements

The two 60 degree networks combined with the three 180 degree networks as shown in Figure 1 form the BFN. Phase, return loss, and insertion loss measurements were taken on the automated test set-up from input ports 1 through 6 to output ports, Σ_1, Σ_2, Δ_1, and Δ_2 for the lower AoA fre-

TABLE I
IDEAL PHASE RELATIONSHIPS

	Element Numbers					
	1	2	3	4	5	6
Σ_1	0	60	120	180	240	300
Σ_2	90	30	330	270	210	150
Δ_1	0	240	120	0	240	120
Δ_2	90	210	330	90	210	330

quency bands and to outputs Σ_1 and Σ_2 for the upper two bands. Table 2 shows the average insertion and range of return losses for the complete BFN, and typical ripple as function of frequency in a single path.

The minimum return loss shown in Table 2 occurred at only one or two frequencies within each band; the average return loss for any signal path was about 18 dB. The insertion losses tabulated include the losses of interconnecting 0.141" semi-rigid cable.

Figure 13 shows plots of both insertion loss and return loss for a signal path in the 12 to 18 GHz BFN. It is pointed out that the loss due to power split in any signal path is 7.78 dB.

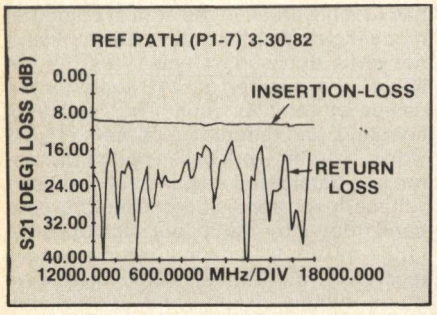

Fig. 13 Stripline BFN response.

BFN Test Results — Phase Measurements

Figure 14 is a plot of phase for the 12-18 GHz BFN for the path port 2 to Σ_1 with reference to path port 5 to Σ_1 (180 degree pair). Figures 15 through 18 are plots for various signal paths in the 4-8 GHz BFN with port 1 to Σ_1 as the reference path. The ideal phase relationship for the various signal paths are tabulated in Table 1. Comparison of the test data with Table 1 indicated the measured phase is within 3 degrees of the ideal phase over the bandwidth of the BFN. Phase deviations for signal paths in the 12 to 18 GHz band were within ±5 degrees from ideal.

TABLE II
BFN PERFORMANCE FOR A TYPICAL SIGNAL PATH: PORTS TO Σ1

Band (GHz)	Return Loss Max. (dB)	Return Loss Min. (dB)	Insertion Loss Above 7.78 dB Average	Typ. Ripple (dB)
0.85 - 2.0	48	14.2	1.5	±0.4
2 - 4	50	15	2.0	±0.3
4 - 8	40	15	1.75	±0.5
8 - 12	32	15	2.25	±0.6
12 - 18	35	14.5	2.8	±0.65

Conclusions

The test results obtained from the BFN's in the various frequency bands proves the practicality and usefulness of the composite phase shifter proposed by Hunton[1]. We

[Continued on page 86]

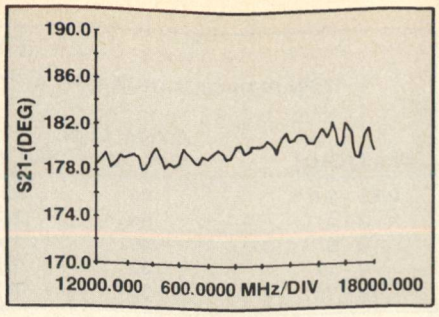

Fig. 14 Phase response for 180-degree pair (ports 2 & 5).

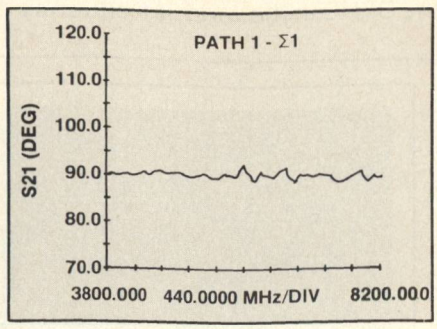

Fig. 15 Phase response from port 1 to E2.

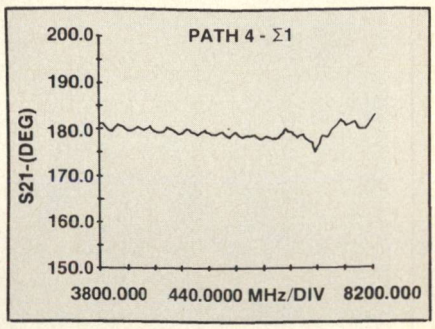

Fig. 16 Phase response from port 4 to E1.

found that the composite phase shift networks are easier to fabricate than networks composed entirely of "C" sections and offer the advantage of very low phase deviation from the desired offset. Partial integration of the quadrature couplers and phase shift networks has given reduced VSWR interaction, and thereby improved overall phase and amplitude characteristics.

Acknowledgements

We would like to acknowledge the contributions of our colleagues at GTE Western Division. Mr. Craig Roberts made valuable contributions in determining the architecture of the BFN; Mr. Joseph Fisher made valuable contributions in design and testing. The patience and skill in assembly and testing by Mr. James Pratali and others led to the successful completion of the BFN project.

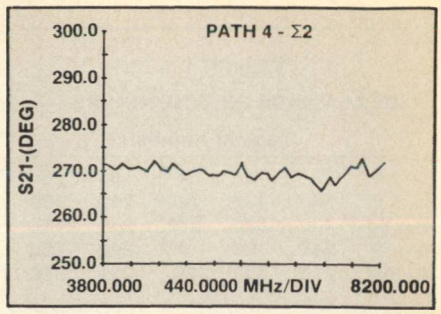

Fig. 17 Phase response from port 4 to E2.

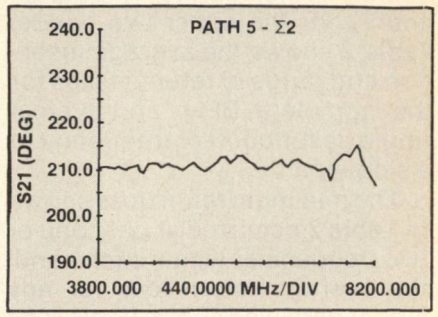

Fig. 18 Phase response from port 5 to E2.

REFERENCE

1. Hunton, J. K., "New Differential Phase Shift Networks Combining All-Pass and Band-Pass Elements", *1981 IEEE MTT-S International Microwave Symposium Digest*, pp. 223-225.

Mr. J. Keith Hunton, is a technical staff specialist in microwave circuit design at GTE Systems, Western Division. His work in this field, which has spanned 35 years, has recently been in the area of computer modeling and optimization of microwave networks and subsystems. This has resulted in a number of CAD tools for the design of complex equalizing, matching, coupling, and differential phase-shift networks. Former work has included transistor, and parametric amplifiers; broadband voltage-tuned transistor oscillators; broadband frequency multipliers; high dynamic range mixers for channelized microwave receivers, microwave filters, microwave diode switch circuits and controllable attenuators.

Robert B. Wilds, received his BSEE from Auburn University in 1950. Since graduation he has been active in the design of a wide variety of microwave and transmission line components with Sandia Corporation, Melpar, Inc., ESL, Inc., and GTE Systems. He has been the author or coauthor of ten technical papers on microwave filters, multiplexers, image rejection mixers, and other microwave topics. At present he is a Senior Engineering Specialist in the Microwave Receiver Department of GTE Systems, Western Division, and is involved in the design and development of multi-octave phase-shift networks and hybrids.

Marshall J. Maple, received his BSEE degree from the University of Akron in 1981. Upon graduation he joined GTE Systems, Western Division, where he works in the Microwave Receiver Group. There he has worked on the design and development of differential phase circuits, couplers, cable equalizers, and software for the design and optimization of such components. ■

Coupler for 94 GHz Network Analyzer

Danilo Radovich
Hughes Aircraft Company
Electron Dynamics Division
Torrance, CA

Introduction

Techniques for measuring complex impedances or scattering parameters of millimeter-wave networks have not been generally available. Such methods are available frequencies. It has been shown, however, that an arbitrary six-port junction can be used to determine explicitly the network parameters of interest. Such a junction may be the key to practical millimeter-wave network analyzers.

Various six-ports have been built with metal waveguide components which gave encouraging results. Constructing such a junction out of discrete metal waveguide components requires multiple waveguide connections which can be troublesome at higher millimeter-wave frequencies. Furthermore, the excessive size of the six-port constructed in this manner does not allow for easy temperature control and stabilization. Using dielectric waveguide as a transmission medium is an alternative approach which overcomes most of the limitations of the metal waveguide.

We will present the development of the six-port network in dielectric waveguide along with the highlights of the theory of dielectric waveguides and couplers. With the basic component being a type of a coupler which is a dielectric analog of a narrow banded short slot hybrid, it was initially believed that this device would be usable only over a narrow frequency range centered at the design frequency. As we shall show, based on the measured amplitude and phase characteristics of a dielectric coupler, this six-port junction actually may be usable over a substantial portion of the millimeter waveguide band.

Dielectric Waveguide

Dielectric waveguide is a transmission medium which supports a discrete set of propagation modes. Because of the abrupt change in permittivity at the air-dielectric interface, dielectric waveguide confines these propagation modes within the dielectric while the fields decay exponentially outside the medium. Figure 1 illustrates the guide geometry and defines the basic parameters of interest for a guide of permittivity ϵ_1 surrounded by permittivity ϵ_0.

By writing Maxwell's equations for the two regions and matching the boundary conditions, the dispersion relationship may be derived. Among several authors who have analyzed this problem, Marcatili [1] and Goell[2] present by far the most complete results. Goell has solved the rectangular boundary value problem in cylindrical coordinates for the most general solution while Marcatili used rectangular coordinates neglecting the fields in the corner regions.

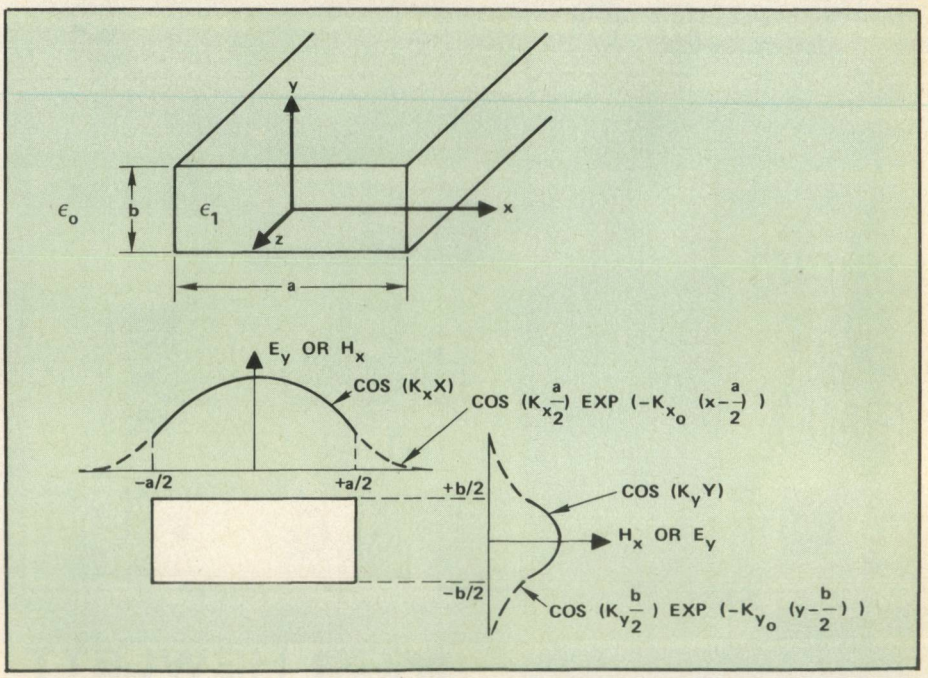

Fig. 1 Dielectric waveguide parameters.

Both approaches produce essentially the same results except in the limit of small values of guide height, b Goell's analysis reveals the true nature of the lowest order modes in that there is no cutoff.

Analysis reveals that the rectangular dielectric waveguide modes are neither pure TE nor pure TM modes. However in the limit of large aspect ratios, short wavelengths and small relative dielectric constant, the transverse electric field is essentially parallel to one of the transverse axis. Modes are, therefore, designated as E^y_{mn} if, in the limit, their electric field is parallel to the y-axis and as E^x_{mn} if, in the limit, their electric field is parallel to the x-axis. The m and n subscripts are used to designate the number of maxima in the x and y directions respectively.

The choice of using E^y or E^x modes is somewhat arbitrary for dielectric waveguide, however the preference is towards E^y modes when interfacing with rectangular metal waveguide. For purposes of simplicity, all further discussions of dielectric guide will be based upon E^y modes with the underlying understanding that E^x modes are equally applicable.

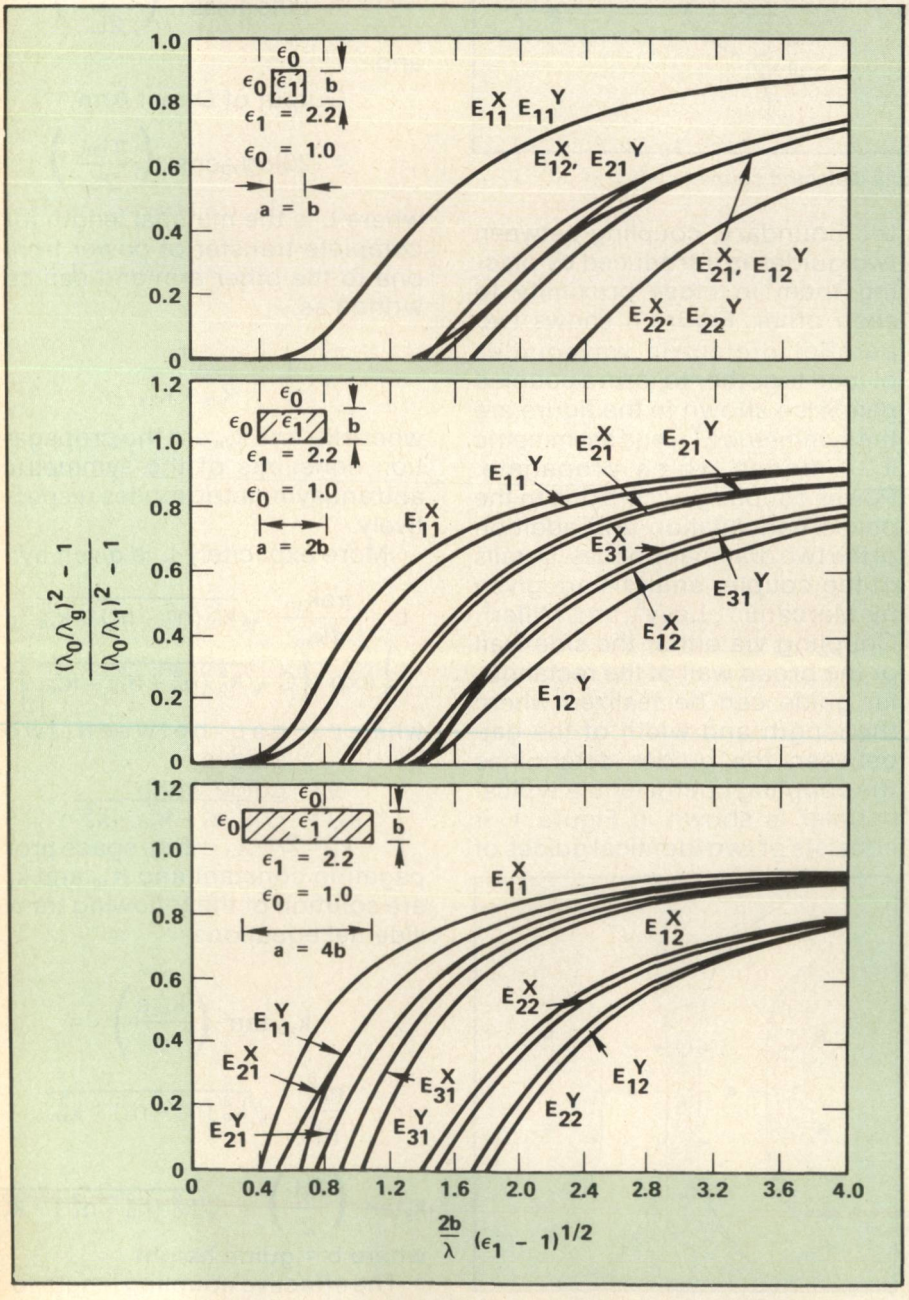

Fig. 2 Propagation characteristics of teflon dielectric waveguide.

The propagation constants for E^y modes in the dielectric guide are given approximately by:

$$k_x = \frac{p\pi}{a} - \frac{2}{a}\tan^{-1}\frac{k_x}{k_{xo}}$$

and

$$k_y = \frac{q\pi}{b} = \frac{2}{b}\tan^{-1}\frac{E_o k_y}{E_1 k_{yo}}$$

where

- p , q are integers denoting mode order
- a , b width and height of guide respectively
- k_x , k_y propagation constants in the x and y directions within the guide respectively
- k_{x_o} , k_{y_0} propagation constants in the x and y directions in the medium surrounding the guide

From these expressions, general dispersion curves can be generated such as those in Figure 2. These curves are plotted for a guide dielectric constant of 2.2 surrounded by air. Goell's analysis has been used to extend the (1,1) mode propagation below that Marcatili's analysis. All higher modes exhibit true cutoff below critical values of $2b/\lambda\,(\epsilon_1-1)^{1/2}$. By designing dielectric guides with a suitable height, b, single mode operation can be assured.

Losses due to the dielectric material can be calculated using the attenuation constant α.

$$\alpha = \frac{2\pi\epsilon_1}{\lambda_0}\tan(\delta)\ R\ (4.343)\ \text{c/B/m}$$

where

- ϵ_1 = relative dielectric constant
- λ_o = free space wavelength
- tan δ = loss tangent of dielectric
- R = scale factor related to amount of energy propagating outside dielectric

R ranges from zero to $1/\sqrt{\epsilon_1}$.[9] $R = 1/\sqrt{\epsilon_1}$ corresponds to plane wave propagation totally in the medium and produces the worst case value of α. For example,

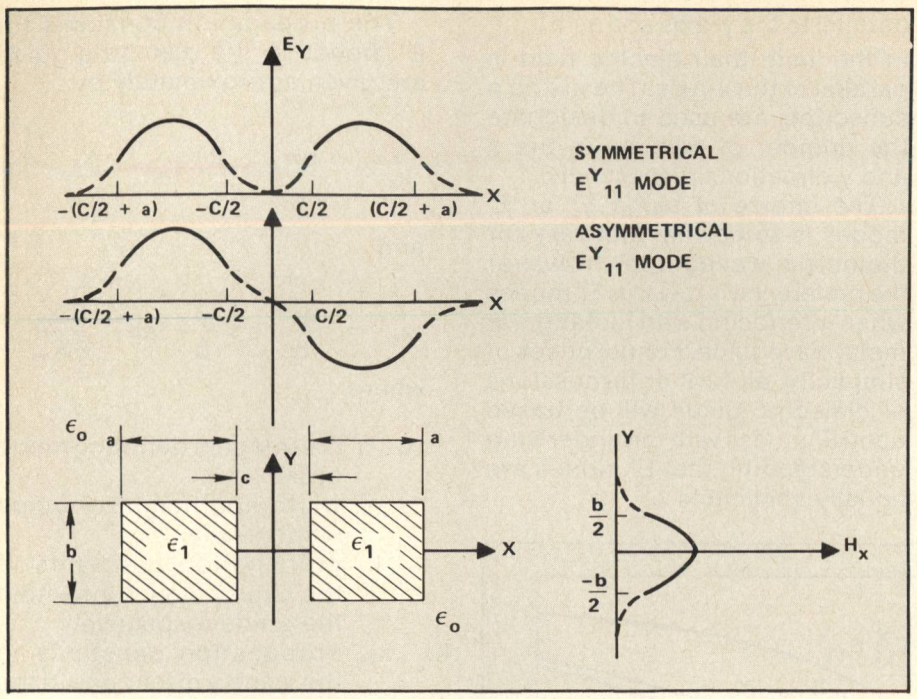

Fig. 3 Field distribution of a dielectric coupler.

Teflon with $\varepsilon_1 = 2.2$ and $\tan\delta = .0002$, $\alpha = 2.5$ dB/m at 94 GHz.

Many materials are suitable for dielectric waveguide and the ultimate choice is application dependant. Because of its low RF loss characteristic as well as its suitable mechanical properties teflon is one of the best choices for constructing integrated circuits. The aspect ratios of the dielectric guides are conveniently chosen to correspond to that of a standard metal waveguide for the frequency band of interest. Well matched transitions from metal to dielectric guide are readily accomplished by tapering the tip of the dielectric guide and inserting it through the electromagnetic horn into the metal waveguide. For teflon guides at 94 GHz transitions such as these have an insertion loss of less than .25 dB and a VSWR of better than 1.20:1, while the insertion loss of the dielectric guides themselves was less than .05 dB per inch. Matched terminations are formed by tapering the end of the dielectric guide and thus launching the RF into the lossy dielectric material. A VSWR of 1.02:1 or better is achieved with such terminations.

Dielectric Coupler

Because the electromagnetic fields extend beyond the dielectric boundary, coupling between two guides is introduced by placing them in close proximity to each other. Figure 3 shows two parallel dielectric waveguides placed together to form a coupled pair. Also shown in the figure are the symmetric E^Y_{11} and asymmetric E^Y_{11} modes which propagate. Power coupling occurs due to the phase cancellation and addition of the two dominant modes. Details of the coupler analysis are given by Marcatili [1], Levy[3], and Miller[4]. Coupling via either the side wall or the broad wall of the rectangular guide can be realized where the length and width of the gap between the guides determines the coupling coefficient. A typical coupler is shown in Figure 4. It consists of two identical guides of

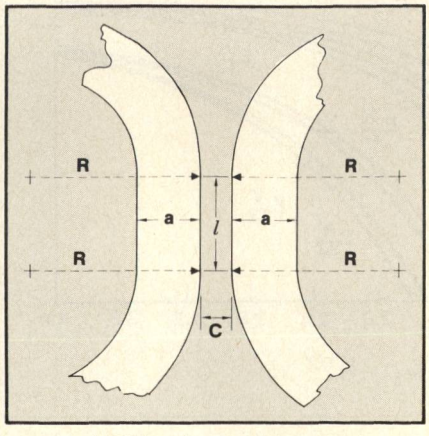

Fig. 4 Dielectric coupler geometry.

cross-section (a × b) curved in such a way that they are within the coupling distance of each other. When calculating coupling coefficient of such a coupler the coupling effect of the curved sections has to be taken into account as well.

Assume that this coupler is made out of material with relative dielectric constant n_1^2 and immersed in a medium of relative dielectric constant n_0^2. The power ratio of output over input in decibels can be expressed as: [5]

$$\text{Output of Coupled Arm} = -20\log_{10}\sin\left(\frac{\pi l_{eff}}{2L}\right)$$

and

$$\text{Output of Direct Arm} = -20\log_{10}\cos\left(\frac{\pi l_{eff}}{2L}\right)$$

where L is the minimal length for complete transfer of power from one to the other arm and can be written as:

$$L = \frac{\pi}{k_{zs} - k_{za}}$$

where k_{zs} and k_{za} are the propagation constants of the symmetric and antisymmetric modes respectively.

More explicitely L is given by:

$$L = \frac{\pi a k_{zo}}{4k_{xo}} \sqrt{k_o^2 (n_o^2 - n_1^2) - k_{xo}^2} \cdot \left\{\exp\left[C\sqrt{k_o^2 (n_o^2 - n_1^2) - k_{xo}^2}\right]\right\}$$

where c = gap between two guides
a = guide width
$k_{zo} = \sqrt{k_o^2 n_1^2 - k_{xo}^2 - k_y^2}$
$k_o = 2\pi/\lambda_o$ = free space propagation constant and K_{xo} and k_y are solution of the following transidental equations:

$$k_{xo}\tan\left(\frac{k_{xo}a}{2}\right) = \frac{n_o^2}{n_1^2}\sqrt{k_o^2 (n_o^2 - n_1^2) - k_{xo}^2}$$

$$k_y \tan\left(\frac{k_y l}{2}\right) = \sqrt{k_o^2 (n_o^2 - n_1^2) - k_y^2}$$

where b = guide height

The effective coupling length to a first order approximation is:

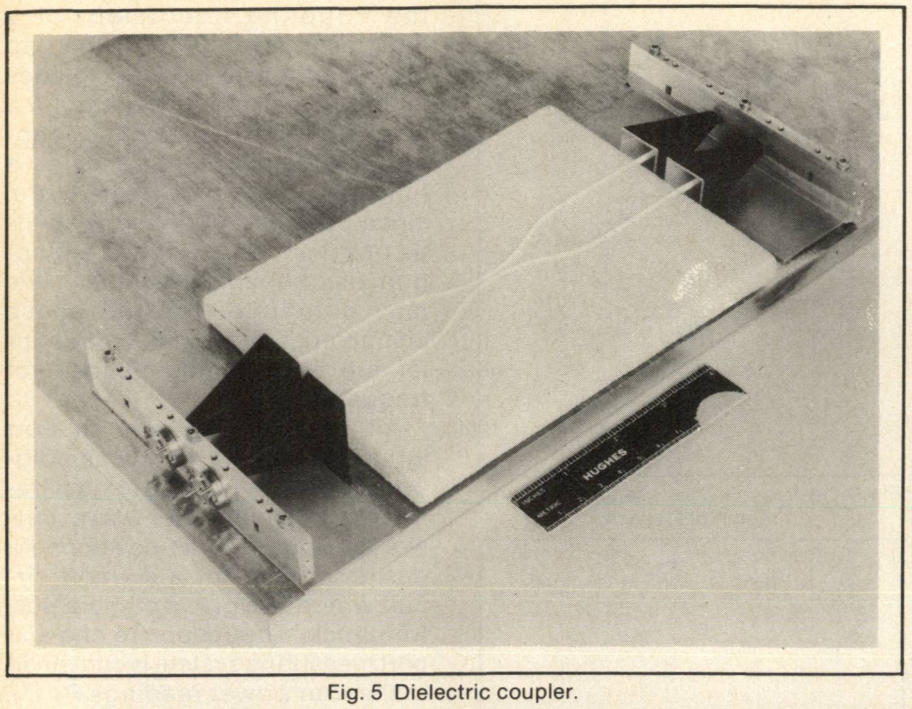

Fig. 5 Dielectric coupler.

$$l_{eff} = l + \frac{2L}{\pi}\int [k_{zs}(z) - k_{za}(z)]dz$$

where the second term is the contribution due to the curved portion of the waveguide. The limits of integration are to be taken from the point where the waveguides start to curve away from the uniform coupling region till they get far enough from each other so that the coupling between them becomes negligible.

In constructing a dielectric coupler, certain practical guidelines have to be observed. For example, as the spacing becomes smaller, the effective coupling length for complete transfer of power becomes shorter, thereby requiring the radius of curvature into the coupling region to be small which increases the radiation loss. For this reason, the interguide spacing should be made as large as practical without adding excessive length to the coupler. It was found experimentally that the measurable radiative loss at 94 GHz occurs when the bending radius gets smaller than two inches which establishes a limit on how small a dielectric coupler can be made at this frequency.

A broadwall hybrid formed using two dielectric guides is shown in Figure 5. The frequency response of such a coupler was measured using the recently developed computer controlled reflectometer which made it possible for the automated scalar transmission and reflection measurements to be taken over a full WR-10 waveguide band. Figure 6 shows the response of the two ports as a function of frequency while Figure 7 shows the response of the coupled port normalized to the direction port. This particular coupler is centered at 96.0 GHz

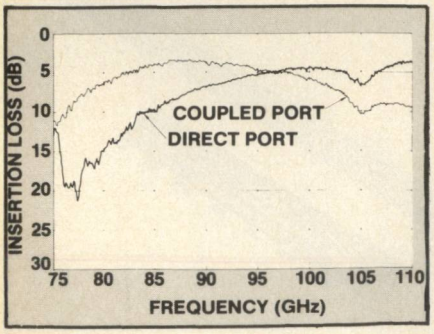

Fig. 6 Frequency response of a dielectric coupler.

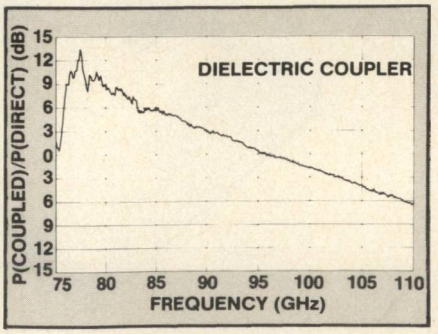

Fig. 7 Coupling ratio for a dielectric coupler.

[Continued on page 94]

where the insertion loss is 2.0 dB. The insertion loss includes propagation loss through the dielectric, launching loss due to transitions from metal to dielectric guides, and radiation loss due to the curvature of the dielectric guides.

The phase characteristics of the dielectric coupler are equally important for six-port application. The phase change as a function of coupling strength was measured by keeping the effective coupling constant and varying the separation between the two guides. In our experiment, phase measurements were taken at the single frequency of 94.0 GHz.

Initially, the separation between the two guides was set to give equal power splitting between the direct and coupling arms. An electrical short was placed in each of the arms an equal distance from the coupling region while the power at the isclation port was monitored. If the coupled RF power undergoes a 90° phase shift relative to the power of the direct arm, then the power of the two arms should, upon reflection from the shorts, recombine into the isolation port. This was found to be the case thus establishing the phase response for a 3 dB dielectric coupler. A phase bridge was used to measure the relative phase of the two arms as a function of coupling coefficient. It was found that the relative phase remained constant at 90° throughout most of the coupling range. Significant deviation occurred when the imbalance between the two arms became greater than 15 dB. In this range, however, the measurement error became too great for reliable data to be taken. The phase change of the direct port as a function of the coupling coefficient was also measured and found

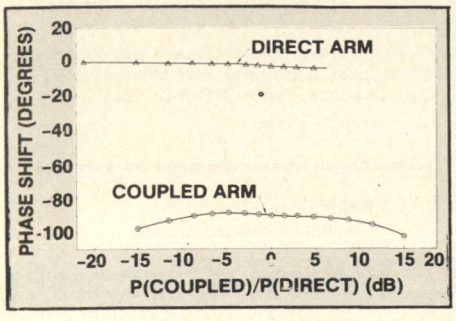

Fig. 8 Phase characteristics of a dielectric coupler.

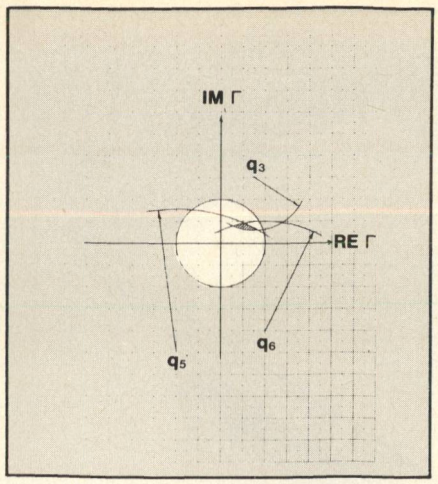

Fig. 9 Desired reflection coefficient within a region of Γ space.

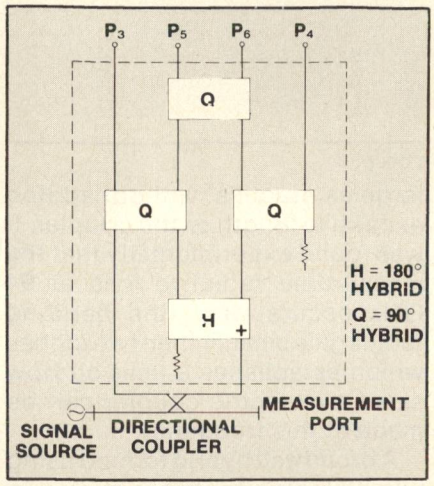

Fig. 10 Six-port circuit.

to be virtually constant since it is within the measurement error of the experiment. Figure 8 shows the results of the phase measurements for both direct and coupled ports.

For the given effective length the coupling coefficient of a coupler is a function of the gap between the two dielectric guides in units of wavelength. Thus, for a given physical gap size, the coupling coefficient will change as a function of frequency. Therefore, since our experiment showed little or no phase change as a function of coupling coefficient, we may conclude that the phase characteristics of a dielectric coupler are virtually independent of frequency.

Although an arbitrary six-port junction can be used to unambiguously determine scattering parameters of millimeter-wave networks, Engen[7,8] has developed a design criteria for a six-port circuit which will give optimum performance. The response of a six-port measuring system is contained in the four power readings P_3, P_4, P_5, P_6. In general, these readings can be expressed in terms of the emergent wave amplitude |b| and the complex reflection coefficient

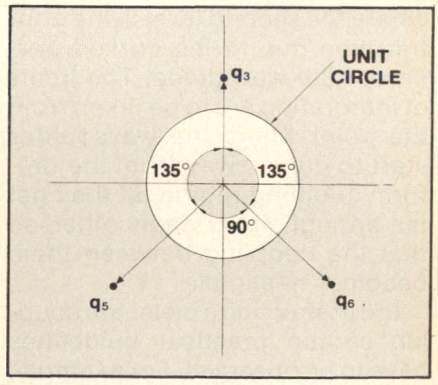

Fig. 11 q distribution of a six-port circuit.

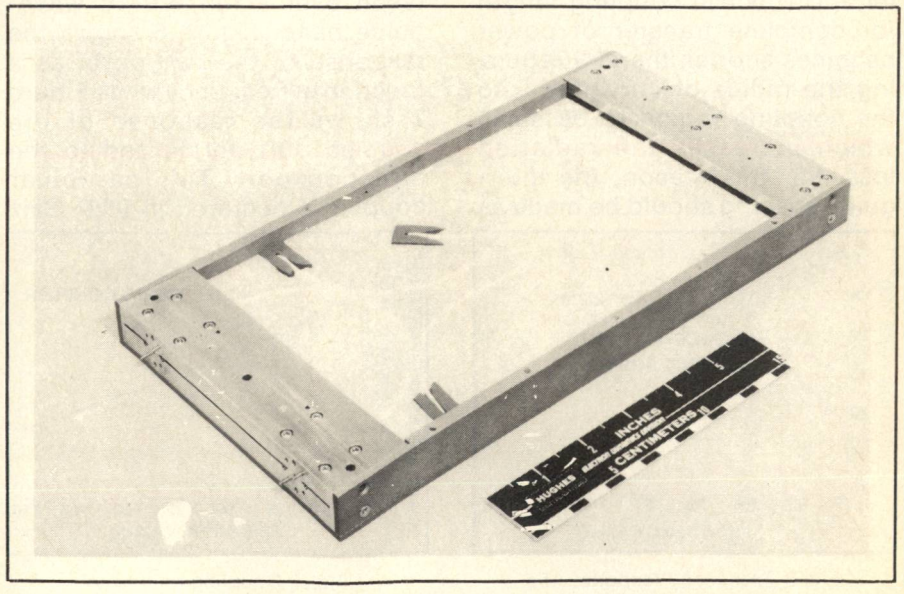

Fig. 12 Dielectric six-port network analyzer.

Γ at the output measurement plane as follows:

$$P_3 = |A|^2|b|^2|\Gamma - q_3|^2$$
$$P_4 = |D|^2|b|^2|1 - \Gamma\Gamma_g|^2$$
$$P_5 = |E|^2|b|^2|\Gamma - q_5|^2$$
$$P_6 = |G|^2|b|^2|\Gamma - q_6|^2$$

The parameters $|A|$, $|D|$, $|E|$ and $|G|$ are scalar proportionality constants and Γ_g, q_3, q_5, and q_6 are complex constants determined by the circuit configuration and the coupling characteristics of the component hybrids. The first design objective is to have $\Gamma_g = 0$. If this condition is satisfied, we may eliminate $|b|$ by dividing P_3, P_5, and P_6 by P_4. After eliminating $|b|$ and rearranging terms, we obtain the following three equations:

$$|\Gamma - q_3|^2 = \left|\frac{D}{A}\right|^2 \frac{P_3}{P_4}$$

$$|\Gamma - q_5|^2 = \left|\frac{D}{E}\right|^2 \frac{P_5}{P_4}$$

$$|\Gamma - q_6|^2 = \left|\frac{D}{G}\right|^2 \frac{P_6}{P_4}$$

These are equations of circles in a complex Γ space centered at respective q's and with the radii proportional to the corresponding power readings.

For an ideal system, these three circles will intersect at one common point, which will correspond to the complex reflection coefficient we set out to find. For a non-ideal system, however, because the power meters have limited accuracy, the desired reflection coefficient can be ascertained only within a certain region of Γ space as shown in the shaded portion of Figure 9.

It is apparent that a better choice of q's than those shown in Figure 9 can be made that will improve the accuracy of the measurement. It is clear that the best results are obtained when the q's are located at the verticies of an equalateral triangle centered at the origin and with magnitudes somewhat larger than unity. This last condition is important if we assume passive terminations where the reflection coefficient is always within the unit circle. Unfortunately a broadband circuit that will yield a 120° phase difference between adjacent q points does not exist which suggests some compromise in the design goals as outlined above.

A circuit that comes closest to satisfying the criteria for optimum performance is shown in Figure 10. This circuit consists of a vector voltmeter portion enclosed within the dotted lines of the figure and a directional coupler which divides the available power between the vector voltmeter and the test port. As shown in the figure, the vector voltmeter consists of three quadrature hybrids and one in-phase power divider. Note that although resistive terminations are shown at two different locations within the vector voltmeter, ideally none of the signal power reaches these; hence, this part of

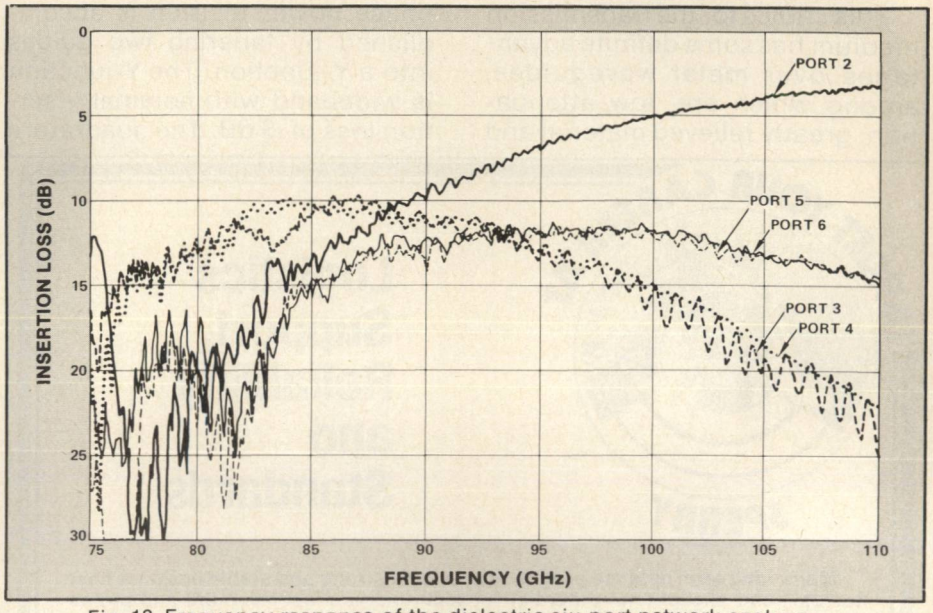

Fig. 13 Frequency response of the dielectric six-port network analyzer.

[Continued on page 96]

the circuit is inherently lossless. The locations of q's for this circuit are shown in Figure 11 where the relative phase differences are 135°, 90°, and 135° and the magnitudes are $|q_5| = |q_6| = 2$ and $|q_3| = \sqrt{2}$. Based on this circuit, a six-port network was developed using teflon dielectric guide.

This choice for the transmission medium has some definite advantages over metal waveguides, among which are: low attenuation, greatly relieved material and mechanical constraints, compactness and low fabrication costs. Figure 12 shows the analyzer interior: the teflon strips are inlaid into low dielectric foam to form an integrated dielectric circuit; the quadrature hybrids are formed by bringing guides in close proximity to each other while the in-phase power division is accomplished by tapering two guides into a Y-junction. The Y-junction is wideband with nominal insertion loss of .5 dB. The quadrature hybrids are centered at 94 GHz and otherwise have the same amplitude and phase characteristics as described in the previous section.

To accomplish transitions from metal to dielectric waveguide, the present design uses a compound horn. With the compound horn, first one dimension of the horn is tapered outward while the other is kept constant, and then the latter dimension is tapered outward while the first is kept constant. When used as a transition, the compound horn performs equally as well as the electromagnetic horn, yet has the advantage of being much less expensive and easier to fabricate since it incorporates all of the necessary transitions in a single-split block.

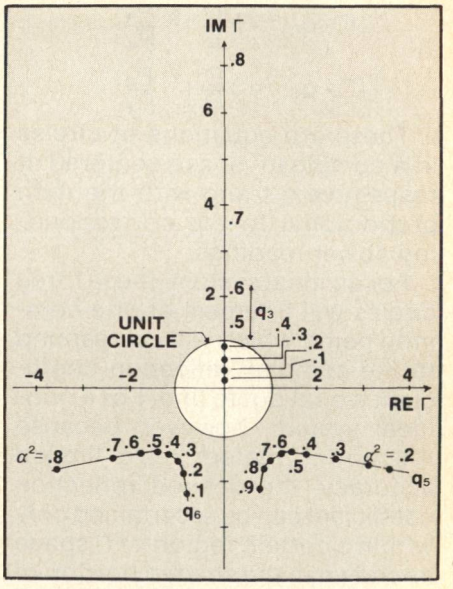

Fig. 14 q distribution for a dielectric network analyzer as a function of the coupling coefficient.

The frequency response of the six-port network was measured across the full waveguide band with the results summarized in Figure 13 where various curves are labeled according to Figure 10. With input power incident into port 1 and the remaining ports terminated into matched loads. The response of each port was taken in turn by sampling its power through a coupled arm of a 20 dB coupler. In this manner the error introduced by the measurement was negligible. The high VSWR exhibited at the lower end of the frequency band is not surprising since the circuit was not

intended to accommodate the full waveguide band. Therefore, care was not taken to provide for the well matched metal to dielectric transitions and dielectric terminations at lower frequencies. Away from this high VSWR region the response of the six-port is as would be expected based on the known response of the component hybrids. At the lower frequencies where we have overcoupling more power goes to ports 3 and 4 while at the higher frequencies where we have undercoupling more power goes to ports 5 and 6.

Since the amplitude response of the dielectric six-port was not very flat, the question that one might ask is, over what frequency band can this device be used to make reliable microwave measurements? The answer depends upon several things, particularly the accuracy and the dynamic range of the power meters used as well as the location of the q points as a function of frequency. Based on the measured amplitude and phase response of the dielectric coupler, we are able to predict the movement of the q points as a function of frequency. Figure 14 shows the respective paths that the q's follow as a function of the coupling coefficient α^2 which can be related to frequency using Figure 7.

For example, as the frequency is swept from 83 to 110 GHz, the coupling coefficient varies from .80 to .20. As shown in the figure, q_5 and q_6 always remain outside the unit circle and the phase between them stays constant at 90°. However, for coupling coefficient of less than .41, q_3 which always stays on the imaginary Γ axis, falls within the unit circle. This may cause some degradation in the accuracy of the measurement if the reflection coefficient happens to fall in the immediate vicinity of q_3. Aside from this possible sacrifice in performance, it seems plausable that our dielectric six-port junction can be used to successfully measure complex reflection coefficients over a substantial portion of the WR-10 waveguide band.

REFERENCES

1. Marcatili, E. A. J., "Dielectric Rectangular Waveguide and Directional Coupler for Integrated Optics", BSTJ, Vol. 48, Sept. 1969.
2. Goell, J. E., "A Circular-Harmonic Computer Analysis of Rectangular Dielectric Waveguides", BSTJ, Vol. 48, Sept. 1969.
3. Levy, R., "Directional Couplers", Advances in Microwaves, Academic Press, New York, 1966, pg. 151ff.
4. Miller, S., "Coupled Wave Theory and Waveguide Applications", BSTJ, 33, May 1954.
5. Solbach, K., "The Calculation and the Measurement of the Coupling Properties Image Lines of Rectangular Cross Section", IEEE Trans. Microwave Theory Tech., vol. MTT-27, pp. 54-58, Jan. 1979.
6. Rudokas, R., and T. Itoh, "Passive Millimeter-Wave IC Components Made of Inverted Strip Dielectric Waveguides", IEEE Trans. Microwave Theory Tech., vol. MTT-24, pp. 978-981, Dec. 1976.
7. Engen, G. F., "The Six-Port Reflectometer: An Alternative Network Analyzer", IEEE Trans. Microwave Theory Tech, Vol. MTT 25, No. 12, Dec. 1977.
8. Engen, G. F., "An Improved Circuit for Implementing the Six-Port Technique of Microwave Measurements", IEEE Trans. Microwave Theory Tech., Vol. MTT 25, No. 12, Dec. 1977.
9. Jablonski, D., "Attenuation Characteristics of Circular Dielectric Waveguide at Millimeter Wavelengths", IEEE Trans. Microwave Theory Tech., MTT 26, No. 9, Sept. 1978. ■

Analysis, Design and Characteristics of X-Band Dielectric Wedge Waveguide Antennas

K.K.S. Jamwal, A. Dhar, Renu Vakil
Department of Physics
University of Kashmir
Srinagar, India

Abstract

This investigation reports the design and analysis of dielectric wedge waveguide antennas and their characteristics in the 8.5 - 11.5 GHz X-band frequencies. The analysis discussed can be successfully utilized in designing high gain, wide null region wedge antennas using various polymers with dielectric constant varying from 2-13.

Introduction

The application of dielectric materials for improving the gain-radiation characteristics is well recognised for various geometrical profiles in the microwave frequencies.[1-3] A dielectric wedge shaped waveguide antenna is characterized by high gain that is often suitable as a feed for parabolic or reflector antennas in minimizing the edge diffractions and reducing spillover loss. Figure 1A shows the H-plane view of a wedge antenna and Figure 1C gives its plane view.

The antenna gain and radiation characteristics depend on the antenna length L_A, the antenna wedge angle ω, length L_ω and the dielectric constant ε_r of the material. The purpose of this investigation is to report some design considerations for the analysis and performance of dielectric wedge waveguide antennas employing polymers. The theory is supported with experimental results obtained at X-band 8.5 - 11.5 GHz frequencies.

Theory and Analysis

Consider a dielectric slab as shown in Figure 1B excited by the incident rf signal in the TE_{10} waveguide mode. At the air-dielectric interface MM′ the incident microwave signal AB undergoes reflection BB′ and refraction BC depending on the refractive index η of the material. Similarly, ray BC excites the reflected and refracted rays CE and CC′ respectively. The path and electric field amplitude of each multiple scattered ray must satisfy the Snell's law. With each successive scattering the rays CC′, FG etc. are more parallel to the X- axis than the incident ray AB. This results in an improvement in directivity and radiation characteristics of this antenna. It is evident that the dimensions and the dielectric constant ε_r of the dielectric should effect the antenna performance.

The analysis given below is aimed toward the design of a high performance dielectric wedge-waveguide antenna taking into consideration the above concept.

In case of reflected ray EF, if $\angle JFE \geq \phi_c$ then the microwave signal will undergo total internal reflection whereas for $\angle JFE < \phi_c$ some microwave signal will be refracted and not contribute to the directivity of the antenna.

The critical angle for internally scattered ray, $\phi_c = \angle JFE$ determines that the rf energy will be directed in the X-direction FG only and this improves the gain-radiation characteristics of the antenna. This angle ϕ_c depends on the dielectric lens refractive index η_L and the antenna wedge angle ω. The

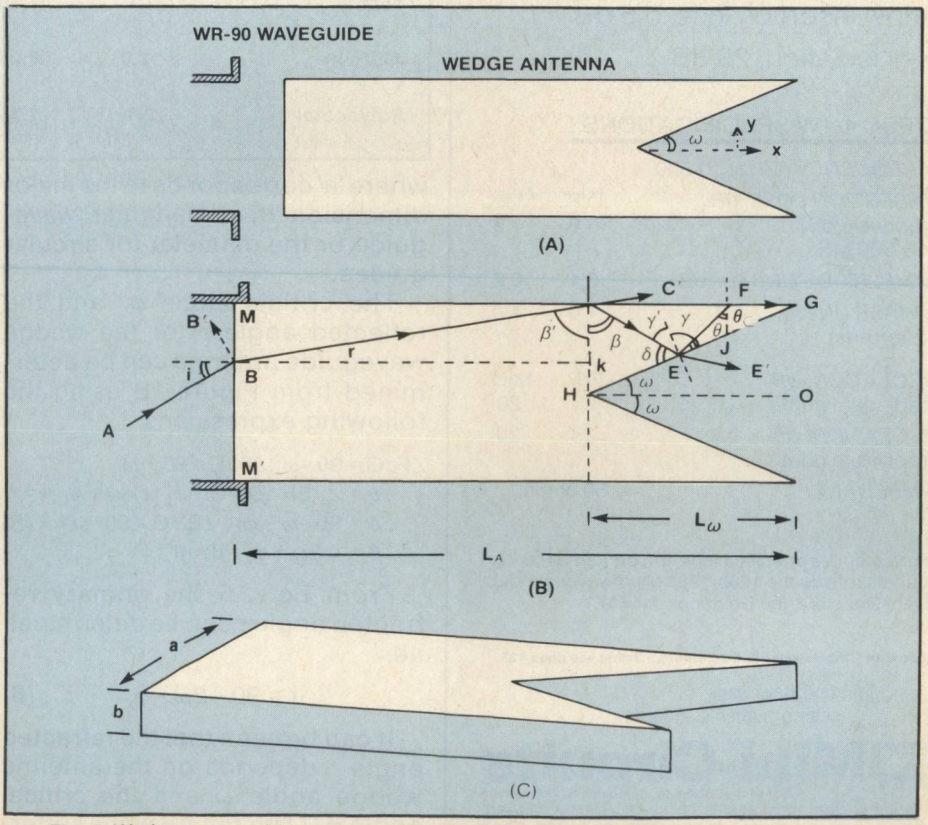

Fig. 1 Wedge waveguide antenna; (A) H-plane view, (B) Schematic for analysis, (C) Plan view.

critical angle and dielectric lens refractive index can be expressed by the relation:

$$\phi_C = \mathrm{Sin}^{-1}(1/\eta_L) \qquad (1)$$

In Eq.1, the dielectric lens refractive index η_L can be determined from the relation[4]

$$\eta_L = 1 + (\eta - 1)\, e^{-(\lambda/\lambda_C')^2} \qquad (2)$$

where η ($=\sqrt{\varepsilon_r}$) is the refractive index of the dielectric material, λ denotes the signal operating wavelength and λ_C' the characteristic wavelength which is very similar to the cut-off wavelength of waveguides in E-plane. The cut off wavelength λ_C' is thus:

$$\lambda_C' = 2\eta a \text{ (for rectangular lenses)} \qquad (3)$$

and

$$\lambda_C' = \frac{\pi\eta a}{1.84} \text{ (for circular lenses)} \qquad (4)$$

TABLE I

WEDGE WAVEGUIDE ANTENNA DESIGN PARAMETERS FOR VARIOUS POLYMERS

f_o = 10.0 GHz: (L_A = 6.5 λ)

Material	ε_r	η_L	ϕ_c	2ω	L_ω
Polypropylene	2.55	1.41	45.17°	20.83°	6.35 cms (2.11 λ)
Perspex (Lucite)	2.56	1.41	45.17°	20.83°	6.35 cms (2.11 λ)
Nylon	2.80	1.47	42.86°	24.17°	5.44 cms (1.81 λ)
Teflon	2.1	1.28	51.38°	12.00°	10.39 cms (3.46 λ)
Alumine	12.0	3.26	17.86°	62.01°	1.90 cms (0.63 λ)
Polyacetal	2.3	1.34	48.27°	16.39°	8.16 cms (2.72 λ)

where 'a' corresponds to the major dimension in rectangular waveguide or the diameter for circular guides.

The critical angle ϕ_C and the reflected angle r for the wedge waveguide antenna can be determined from Figure 1B using the following expressions:

$$\angle FJG = 90 - \omega;\ \angle FJE = 90 + \omega$$
$$\theta = \angle JEF = 90 - \omega - \phi_C;\ r = \omega + \phi_C;\ r = r'$$
$$\delta = 90 - \omega - \phi_C;\ \angle EHC = 90 - \omega \qquad (5)$$
$$\beta = = 2\omega + \phi_C;\ \beta = \beta'$$

From Eq's. 5 the primary refracted angle r can be determined i.e.

$$r = 90 - 2\omega - \phi_C \qquad (6)$$

It can be seen that the refracted angle r depends on the antenna wedge angle ω and the critical angle ϕ_C. The ray AB while suffering refraction along BC has to satisfy the Snell's law i.e.:

$$(\mathrm{Sin}\ i / \mathrm{Sin}\ r) = \eta_L \qquad (7)$$

Substituting for r from Eq. 6 one finds that:

$$\mathrm{Cos}\,(2\omega + \phi_C) = \mathrm{Sin}\ i / \eta_L$$
$$\text{i.e. } \mathrm{Cos}\,(2\omega + \mathrm{Sin}^{-1}(1/\eta_L)) = \mathrm{Sin}\ i/\eta_L \qquad (8)$$

Eq. 8 must be satisfied to achieve ideal antenna characteristics which takes into account the wedge angle ω, critical angle ϕ_C, dielectric constant ε_r, lens refractive index η_L, microwave signal wavelength λ and forms the basis of antenna design.

Antenna Design

Let us consider the design procedure for a polypropylene dielectric (ε_r = 2.55 at 10.0 GHz) wedge waveguide antenna for X-band application with the centre-frequency located at 10.0 GHz (i.e. λ = 30 mm wavelength) and launched from a standard X-band WR 90 waveguide having internal dimensions 'a' = 22.86 mm and 'b' = 10.16 mm.

Since $\eta = \sqrt{\varepsilon_r} = 1.60$, the cut off wavelength λ_C' and η_L can be determined from Eqs. 3 and 2 respectively, i.e. $\lambda_C' = 73.15$ mm and $\eta_L = 1.41$. Next, the critical angle for optimum rf energy directed in the X-axis can be determined from Eq. 1, i.e.:

$$\phi_C = \mathrm{Sin}^{-1}(1/1.41) \cong 45.17$$

and this value substituted in Eq. 8 yields:

$$\mathrm{Cos}\,(2\omega + 45.17) = \mathrm{Sin}\ i/1.41 \qquad (9)$$

which shows that the antenna wedge angle depends on the incident microwave signal angle 'i'.

Our investigations have shown

that to realize satisfactory antenna characteristics the incident angle varies from 30° - 40°, whereas i = 35° gives a compromise for the antenna in X-band frequencies. Substituting this value of incidence angle in Eq. 9 gives:

$$\omega \cong 10.41° \qquad (10)$$

as the desired wedge angle. Since the antenna utilizes a rectangular profile with a = 22.86mm, it is easy to determine the wedge length L_ω that will result in $2\omega = 20.83$ as shown in Figure 1B. The Δ CHG is being considered here with CG = $L_{\omega i}$ ∠CGH = ω and CH = a/2.

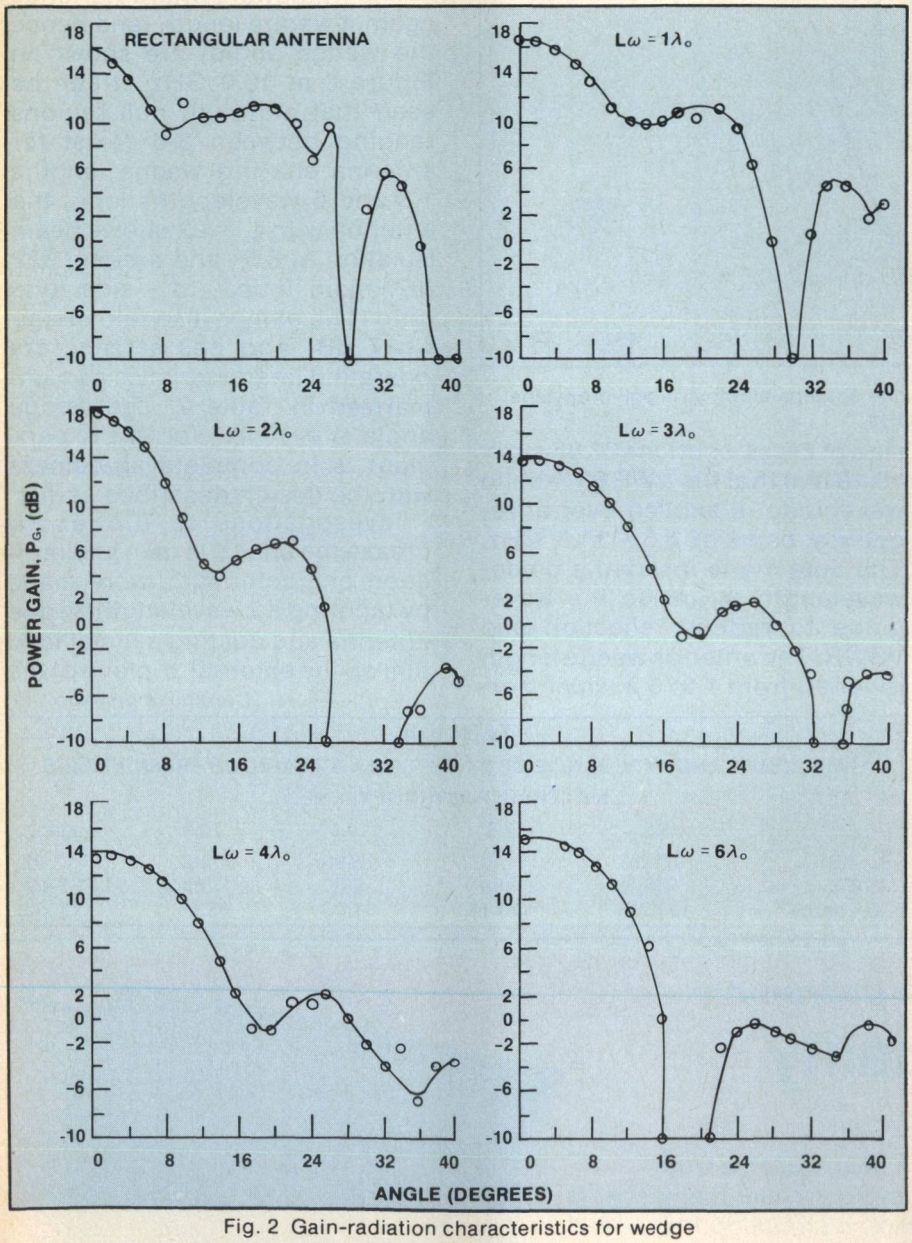

Fig. 2 Gain-radiation characteristics for wedge antenna as a function of wedge lengths L_ω.

TABLE II

P_G, θ_E, VSWR AND Z_A AGAINST ANTENNA WEDGE LENGTH L_ω
MATERIAL: POLYPROPYLENE @ 10.0 GHz.

L_ω	1.0	2.0	3.0	4.0	5.0	6.0	(λ)
Wedge angle, ω	44	22	16	11	10	8	(deg)
P_G,	15.9	16.6	13.3	12.7	12.6	14.1	(dB)
-3 dB beamwidth	14.8	12.4	24.0	20.8	14.8	17.6	$(\theta_E)°$
$G\theta^2$ product	8,600	7,000	12,100	8,100	4,000	8,100	
VSWR	1.3	2.0	2.4	2.1	2.1	1.67	
Z_A,	47.5-j(25)	50-j(35)	62.5-j(49)	55-j(36)	48-j(36)	53-j(25)	
$\|(Z_A)\|$	53.7	61.0	79.1	65.5	59.7	58.1	(ohms)

[Continued on page 102]

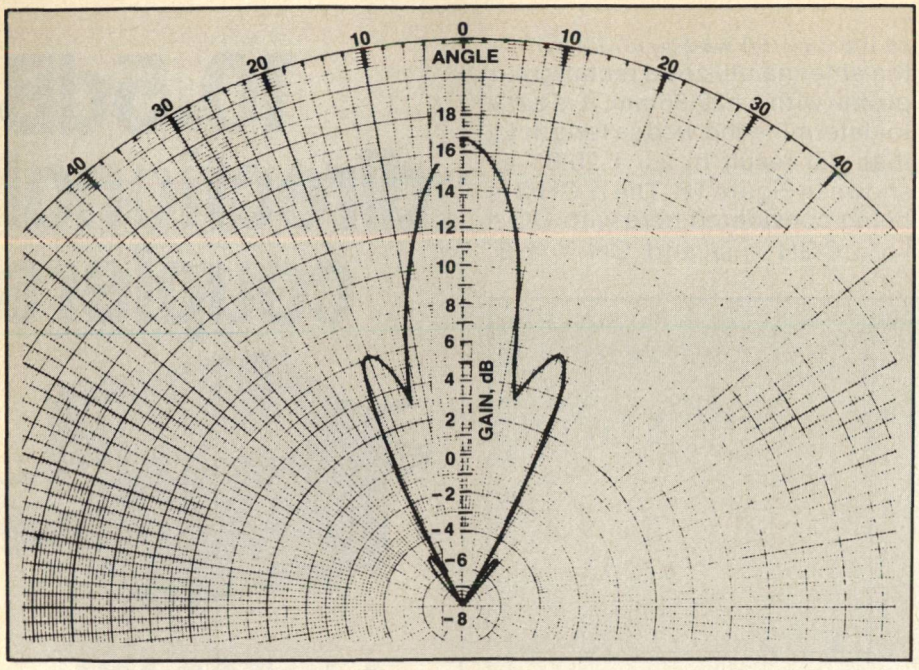

Fig. 3 Radiation characteristics of a 2 λ wedge antenna employing polypropylene at 10.0 GHz.

Therefore,

$L_\omega = (a/2)/\tan \omega \cong 6.35$ cms (11)

It has been established that the dielectric antennas with lengths ranging between 5-7 wavelengths realize gains exceeding 15 dB and small half-power beamwidths ($\leq 20°$)[3]. The antenna length L_A considered in this study is 6.5 λ. Table 1 gives the antenna parameters for various dielectrics[5] for antenna applications in the X-band frequencies.

Experiment and Results

A 6.5 wavelengths (20.0 cms) long polypropylene rectangular slab of cross-sections 22.86 mm x 10.18 mm that fits a WR 90 X-band waveguide is excited over a frequency band of 8.5 - 11.5 GHz. The antenna is inserted a guide-wavelength λ_g inside the waveguide to reduce reflection and VSWR. The antenna wedge length is varied from 1 to 5 λ which corresponds to varying the wedge angle from 44° - 8° respectively, and the antenna relative gain P_G, half-power beamwidth θ_E and, radiation characteristics, VSWR and the impedance measurements are carried out in the entire 8.5 - 11.5 GHz frequencies. Table 2 shows these measurements at 10.0 GHz.

The radiation characteristics against wedge length (and hence the wedge angle) are shown in Figure 2 at 10.0 GHz. It can be seen that although null regions ranging between 3-6° exist for antenna shaving wedge lengths 1,3 and 6 wavelengths long, the antenna with $L_\omega = 2\lambda$ shows beam isolation of 8.5° and a high ($\geq$22 dB) main lobe - to - side lobe ratio. The gain is also fairly large ($\geq$17 dB) and has satisfactory operating characteristics as summarized in Table 2. The wedge angle $\omega \cong 10.41°$ for this experiment is in complete agreement with the design described earlier.

Investigations to further increase the effective gain and radiation characteristics were made by tapering a 2 wavelength wedge antenna and coating a metallic Al film on the external 'b' plane of the

[Continued on page 149]

TABLE III

GAIN, VSWR AND IMPEDANCE OF 2λ ANTENNA AT VARIOUS FREQUENCIES

MATERIAL:POLYPROPYLENE

	8.5	9.5	10.0	10.5	11.5
P_G, dB	17.31	17.40	16.58	14.62	11.93
VSWR	2.6	4.00	2.0	1.23	3.48
$\|Z_A\|$ ohms	121.75	120.41	61.03	55.81	138.06

Practical Millimeter-Wave Ferrite Phase Shifters

Charles R. Boyd, Jr.
Microwave Applications Group
Santa Maria, California

Introduction

Microwave phase shifters find important application as control elements for electronically adjusting the radiation pattern of antennas, and especially for electronically scanning the main beam. With increasing complexity and sophistication of millimeter wave systems, demand has developed for some means of achieving electronic scanning antennas. The logical first choice is to examine techniques proven at lower microwave frequencies for possible utility in the millimeter-wave region. Competing technology for phase shifting devices exists at lower frequencies between units using junction diodes as the variable element, and units using ferrimagnetic material. The general trend is for ferrite-based units to increase in weight, cost, and temperature sensitivity compared with diode-based units as frequency is lowered. On the other hand, diode-based units tend to increase in loss, loss modulation, and cost relative to ferrite-based units as frequency is increased. Ferrite-based units can generally be designed to provide greater phase accuracy at larger amounts of average and peak power than diode-based units, within a given unit cost constraint. Ferrite-based units are not practical below about 2 GHz. The "overlap" region for diode and ferrite phase shifters extends from S-band through X-band, with phase accuracy, power handling, and other specific system requirements determining choice of technology.

At millimeter-wave frequencies, the current state-of-the-art clearly favors ferrite phase shifters. Principal types of ferrite phase shifters currently available at X-band are (a) "twin-slab" latching transverse-field torroid type, (b) 'dual-mode" latching longitudinal-field type, (c) "rotary field" nonlatching transverse-field type. The twin slab design provides nonreciprocal phase shift, which may not conform with system requirements. Furthermore, the tiny toroid size and difficult dimensional tolerance needs for this type rule out conventional processing methods. The rotary-field design is more complicated and requires that a large transverse quadrupole field be produced in a ferrite rod of smaller and smaller diameter with increasing design frequency. For this reason, the "conventional" rotary-field approach is not considered to be feasible at frequencies exceeding approximately 20 GHz.

This leaves the dual-mode geometry as the most attractive approach for millimeter-wave phase shifters. In this class of device, phase shift is obtained by varying the magnitude and direction of a remanent longitudinal magnetic field in a round or square ferrite rod that is metallized to form a fully-filled waveguide. Linearly polarized RF energy is introduced into the ends of the rod from connecting waveguide structures, and is converted into circular polarization by means of nonreciprocal quarter-wave plate sections. These sections are created through the use of transverse quadrupole magnetic field bias near the ends of the ferrite rod provided by permanent magnets.

The metallized ferrite rod is capable of supporting two orthogonal "dominant" modes, e.g. right-hand and left-hand circularly polarized quasi-TE_{11} modes for a round rod. When a longitudinal magnetic bias field exists in the variable-phase section of the rod, the insertion phase increases for one sense of circular polarization and decreases for the other. The insertion phase through the rod is antisymmetric with respect to the bias field direction and the sense of polarization; i.e., the same insertion phase is obtained if the direction of the bias field and the sense of polarization are both reversed. The nonreciprocal quarter-wave plates produce opposite senses of polarization in the two directions of propagation and the bias field direction is intrinsically opposite, hence the insertion phases for an ideal dual-mode phase shifter are equal for all settings of the longitudinal bias field level. In actual devices, small errors in the quarter-wave plates, in the structure symmetry, and in material homogeneity will cause minor deviations from absolute reciprocity.

Theoretical Performance

In its up-to-date realization[1, 2], the Dual-Mode Ferrite Phase Shifter presents a simple cross-section to RF waves; i.e., that of a completely filled circular or square waveguide. Previous literature[3] has pointed out that this simplicity of shape is more conducive to the fabrication of millimeter-wave phase shifters than the relatively more complicated RF structure of the nonreciprocal ferrite phase shifter using a toroid positioned along the axis of a rectangular waveguide. Furthermore, computational results indicate that the dual-mode configuration ought to have intrinsically lower insertion loss than the nonreciprocal toroid configuration, under the constraints of material properties that exist for millimeter-wave applications.

The analytical approaches used to compare performance of the two types of phase shifters were taken from previously reported work. For the dual-mode case, modified transmission line techniques[4, 5] were used to determine the phase shifter and nonreciprocal polarizer lengths in circular

waveguide, constrained in diameter such that the TE_{21} mode was non-propagating. The nonreciprocal toroid case was computed using a transverse resonance method[6], with the waveguide height taken as that of a standard waveguide in each frequency band calculated, and the toroid dimensions and waveguide width adjusted for a uniform phase shift vs. frequency characteristic. Perturbational methods were used in both cases to determine the contributions of waveguide wall loss and material dielectric and magnetic losses to the total predicted insertion loss of phase shifter. The computer programs for each phase shifter type have been used for a number of years in design and performance calculations, and provide results in good agreement with experimental data, at frequencies below the millimeter-wave region.

At frequencies from S-band through X-band, it is common practice to choose a ferrite material for best compromise between insertion loss, temperature stability, power handling capability, size, weight, and cost of the phase shifter. A wide range of material characteristics is available with respect to magnetic activity, peak power threshold, temperature compensation, hysteresis loop squareness, and dielectric constant, such that meaningful trade-off considerations can be evaluated. In the millimeter-wave region, however, the choice of materials is much more restricted. A major consideration is the fact that the saturation magnetization of isotropic square-loop ferrites is limited to around 3000 gauss for magnesium ferrites, and around 4500 gauss for lithium ferrites. These magnetization values yield low relative magnetic activity at 35 GHz and higher frequencies. As a consequence, peak-power threshold is generally not a design consideration using these materials. Of greater concern is the tendency for the dielectric constant, dielectric loss tangent, and stress sensitivity of lithium ferrites to be higher than that of magnesium ferrites. These properties require a small cross-section for the phase shifter, with potentially higher wall loss and dielectric loss. For these reasons, a 3000 gauss magnesium ferrite was chosen as the material for all computations at 35 GHz and above.

Computations were carried out in the 10, 35, 60 and 94 GHz frequency regions for the dual-mode type phase shifter, as well as for two slightly different versions of the non-reciprocal toroid type. One of these latter versions was based on the use of a dielectric filler inside the toroid with dielectric constant similar to the ferrite, the other based on the use of a filler of 30 relative dielectric constant. The X-band (9-10 GHz) designs were calculated using a standard yttrium garnet material of 1600 gauss saturation magnetization. Frequency-dependent matching transformer loss was assumed to bring the calculated performance into line with experimental data.

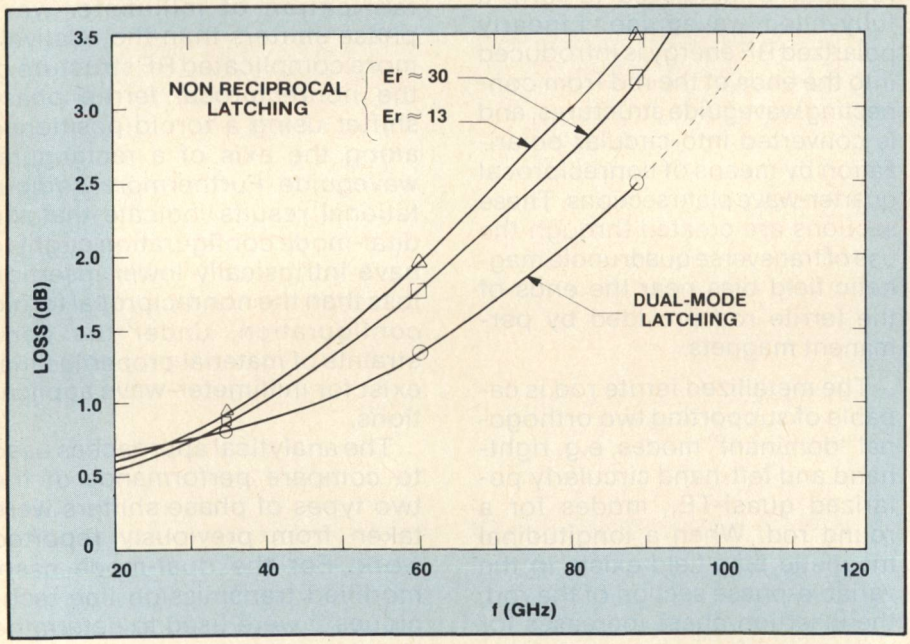

Fig. 1 Comparison of base loss levels for latching ferrite phase shifters.

The results of these computations are summarized in the curves of Figure 1, which compare the base loss levels for the three versions of latching ferrite phase shifter. These curves show clearly that the nonreciprocal toroid-type phase shifters have a slight advantage over the dual-mode type at frequencies below 20 GHz, but that the expected base loss of the dual-mode type becomes progressively less than that of the nonreciprocal types as the frequency is increased above 30 GHz. Both phase shifter types exhibit an increase of base loss with frequency, of course.

A detailed examination of the components of loss gives a clue as to the reason for the theoretically superior performance of the dual-mode type at higher frequencies. Basically, the competely-filled guide geometry of the dual-mode unit is somewhat inefficient with respect to ferrite utilization, i.e., a relatively low fraction of the ferrite produces most of the phase shift[7]. The poorly utilized ferrite does contribute to the magnetic loss, however. On the other hand, the wall current distribution is simply that of a uniformly filled circular waveguide. This contrasts with the nonreciprocal toroid type unit, in which ferrite utilization is very high, and wall currents are concentrated in the regions where the toroid contacts the waveguide surfaces.

Under the constraint that the saturation moment of the ferrite cannot be scaled in proportion to frequency, the tendency will be for the magnetic loss to decrease with increasing frequency, at the expense of higher dielectric and conductive losses. Since the magnetic loss contribution is already low in the nonreciprocal toroid type, a further reduction of this factor does not significantly compensate for the increases in conductive and dielectric losses at

increasing frequency. The opposite is true for the dual-mode unit, which benefits more from the reduction of magnetic loss with frequency.

Practical 35 GHz Units

A 35 GHz dual-mode phase shifter design with characteristics suitable for system applications now exists. The basic configuration for this design is essentially scaled from larger production-type X-band dual-mode phase shifters. A round rod geometry is used for the RF ferrite filled waveguide for several reasons. First of all, the round rod geometry permits operation at larger cross-section than a square rod geometry without introducing unavoidable spurious-mode responses. Also, it is the most convenient shape for millimeter-wave size rods, since the round cylinder can be machined to high precision by centerless grinding.

Table 1 gives a summary of measured performance characteristics for a pilot production run of several hundred 35 GHz units. In addition, Figure 2 shows a fairly typical plot of insertion loss and return loss data, taken by scanning the phase shifter through all states while slowly sweeping frequency between 34 and 36 GHz. In this way, the entire envelope of possible values is mapped. These amplitude measurements were made using a standard reflectometer/ratio meter test set-up. Phase data were measured with a Hewlett-Packard 8410 Network Analyzer/R8747A Downconverting Bridge arrangement.

TABLE 1

SUMMARY OF 35 GHz PHASE SHIFTER PERFORMANCE

Frequency Range	34.0 to 36.0 GHz
Insertion Loss	0.8 dB minimum 1.0 dB typical
Return Loss	20 dB typical
Latching Phase Shift Range	
20°C	430° typical
50°C	400° typical
RMS Phase Error, (Optimum Drive)	
20°C	2.3° typical
50°C	2.5° typical
Switching Time, (Reset-Set Cycle)	55 μs maximum

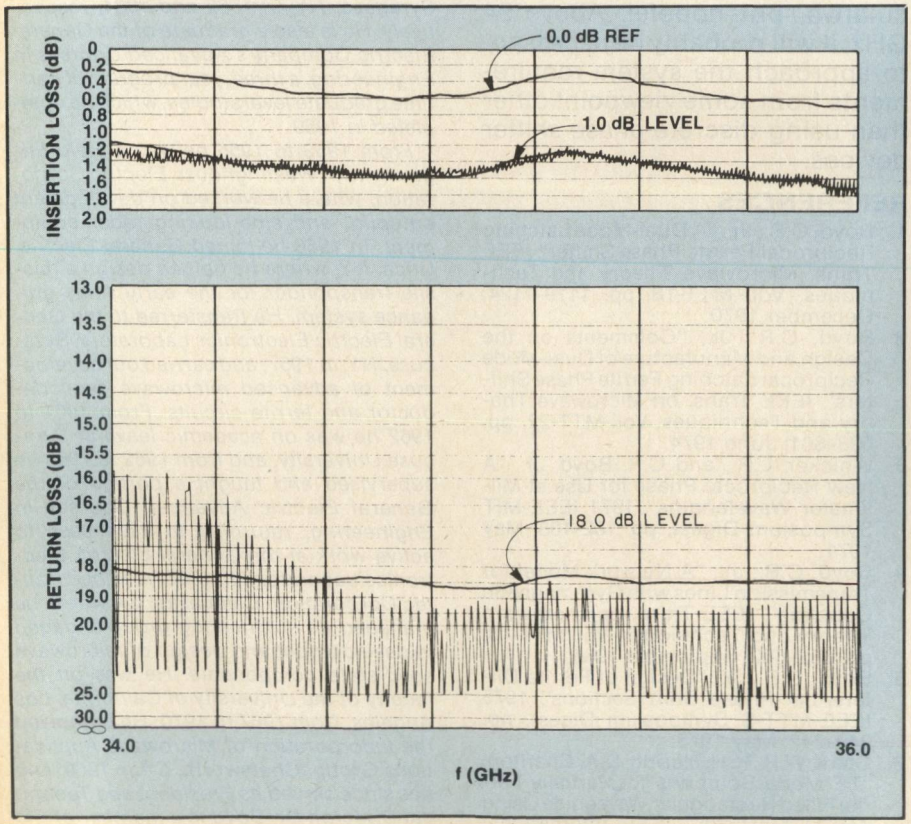

Fig. 2 Typical plot of insertion loss and return loss data.

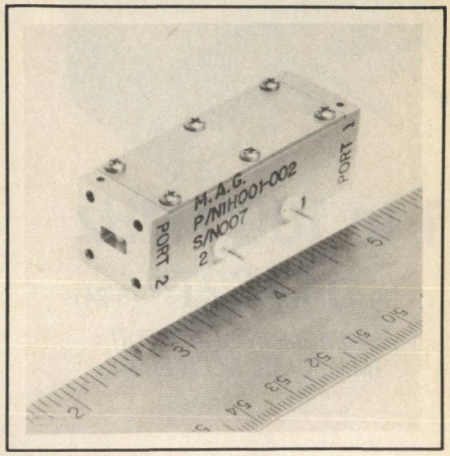

Fig. 3 35 GHz dual-mode phase shifter.

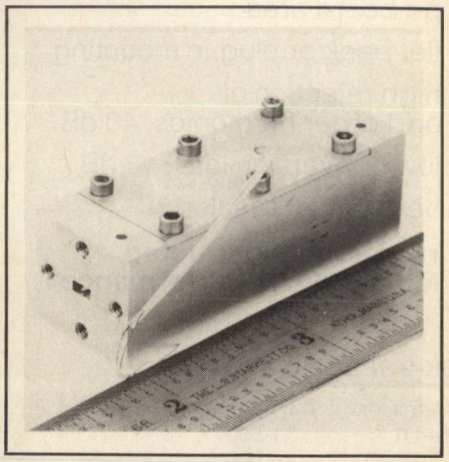

Fig. 4 Experimental 60 GHz phase shifter.

Exclusive of housing, these units are about 0.26 inch in diameter, roughly two inches long, and weigh about a quarter ounce each. Aside from extra care in handling the smaller, more fragile parts, no difficult or exotic processes are required. With adequate tooling, cost to build and test large quantities of 35 GHz units should be comparable to that for X-band dual-mode units.

Units at 60 GHz and Higher Frequencies

Scaling the dual-mode phase shifter to higher frequencies presents the following set of problems:

[Continued on page 108]

[From page 107] **PHASE SHIFTERS**

- The ferrite rod diameter reduces in proportion to frequency, while the rod length remains constant. At some point, a "ferrite toothpick" too fragile to machine or handle is required.
- The magnetic return path elements have similar or worse handling problems than the ferrite rod.
- The nonreciprocal polarizers at each end of the latching region use permanent magnets to produce a transverse fourpole field in the rod. The magnets and rod must decrease in size while the field intensity remains constant.

An experimental 60 GHz unit has been demonstrated[8], with base insertion loss on the order of 1.5 dB and a latching phase shift amount just over 360 degrees. With significant further effort on optimizing the configuration, it should be feasible to produce quantities of units at 60 GHz with electrical, mechanical, and cost parameters suitable for system applications, although the manufacturing attrition would certainly be higher than at 35 GHz. Construction of operating units at 94 GHz is speculative, but hopeful. Above 94 GHz, it will probably be necessary to approach the system requirements from some viewpoint other than using discrete phase shifter devices.

REFERENCES

1. Boyd, C.R., Jr., "A Dual-Mode Latching Reciprocal Ferrite Phase Shifter", IEEE Trans. Microwave Theory and Techniques, Vol. MTT-18, pp. 1119-1124, December 1970.
2. Boyd, C.R., Jr., "Comments on the Design and Manufacture of Dual-Mode Reciprocal Latching Ferrite Phase Shifters", IEEE Trans. on Microwave Theory and Techniques, Vol. MTT-22, pp. 593-601; June 1974.
3. Whicker, L.R., and C.R. Boyd, Jr., "A New Reciprocal Phase for Use at Millimeter Wavelengths", 1971 IEEE-MIT Symposium Digest, pp. 102-103; May 1971.
4. Boyd, C.R., Jr., "A Network Model for Transmission Lines with Gyromagnetic Coupling", IEEE Trans. on Microwave Theory and Techniques, Vol. MTT-13, pp. 652-662, September 1965.
5. Boyd, C.R., Jr., "Design of Ferrite Differential Phase Shift Sections", 1975 IEEE-MTT-S Symposium Digest, pp. 240-242; May 1975.
6. Clark, W.P., K.H. Hering, D.A. Charlton, "TE-Mode Solutions for Partially Ferrite Filled Rectangular Waveguide Using ABCD Matrices", IEEE International Convention Record, Vol. 14, Part 5, pp. 39-48; March 1966.
7. Bell, H.C., Jr., and C.R. Boyd, Jr., "Optimum Filling of Ferrite Phase Shifters of Uniform Dielectric Constant", IEEE Trans. on Microwave Theory and Techniques, Vol. MTT-22, pp. 360-364; April 1974.
8. Boyd, C.R., Jr., "A 60 GHz Dual-Mode Ferrite Phase Shifter", 1982 IEEE-MTT-S Symposium Digest, pp. 257-259; June 1982.

Charles R. Boyd, Jr. *received the B.S.E.E. Degree from Carnegie Institute of Technology, Pittsburgh, PA, in 1953 and the M.E.E. and Ph.D. Degrees in Electrical Engineering from Syracuse University, Syracuse, NY, in 1962 and 1964, respectively. He is also a graduate of the General Electric Company's Advanced Courses in Engineering, a three-year program of part-time graduate level studies, which he completed in 1959.*

From 1953 to 1956 he was a Field Engineer with Westinghouse Electric Corporation, where he worked on development autopilot and side-looking radar equipment. In 1956 he joined General Electric, Utica, NY, where he helped design a missile transponder for the early Atlas guidance system. He transferred to the General Electric Electronics Laboratory, Syracuse, NY, in 1957, and carried out development of advanced microwave semiconductor and ferrite circuits. From 1961 to 1962 he was on academic leave at Syracuse University, and from 1962 to 1963 he supervised and taught a portion of the General Electric Advanced Courses in Engineering, returning in each case to active work at the General Electric Electronics Laboratory. In 1965 he joined Rantec Corporation, Calabasas, CA where he managed an engineering group engaged in development and design of microwave solid-state components. He was on the faculty of the University of California, Los Angeles, from 1967 to 1970. He organized the incorporation of Microwave Applications Group, Chatsworth, CA in 1969, and has since served as President and Technical Director. Dr. Boyd is a member of Eta Kappa Nu and is a licensed Professional Engineer in the State of New York. ■

Design and Development of an Omnidirectional Antenna With a Collinear Array of Slots

P. Volta
Selenia S.p.A.

Introduction

Omnidirectional array antennas are often used in sidelobe suppression secondary surveillance radars for air traffic control or in radio communication systems. This article deals with the design and experimental results of an omnidirectional antenna in vertical polarisation, at a frequency centered at 1030 MHz, realised with a collinear series fed array of annular slots. These slots extend outside as skirts forming half wave dipoles.[1] Mutual coupling between elements is low for two reasons. Free space radiation coupling is minimized by the fact that the axis on which collinear array dipoles lay is the same of their radiation nulls.

Also mutual coupling originated by surface waves running on external conductors is attenuated (but not completely as we will see later) by quarter wavelength chokes inside the dipoles or at array extremities (Figure 1).

For a good design one has to consider that the chokes, formed in the internal parts of dipoles, are efficient if the extremities of contiguous radiating elements have a distance a fraction of wavelength. Silver[2] indicates a distance p = 0.15 λ as an optimum value for it. If choke depth is not enough to reach the required value (nominally $\frac{\lambda}{4}$) the chokes can be partially filled with dielectric rings.

So as a first approximation it is possible to neglect mutual coupling, namely mutual impedences between elements and leaky-wave irradiation, but this will be checked experimentally later. Now these basic problems are to be faced for the antenna design:

- Synthesize the linear array to obtain the desired vertical (E plane) pattern.
- Match the input impedance of the antenna to that of the feeding line.
- Design the radiating element as a module which fits the constraints (a) and (b).

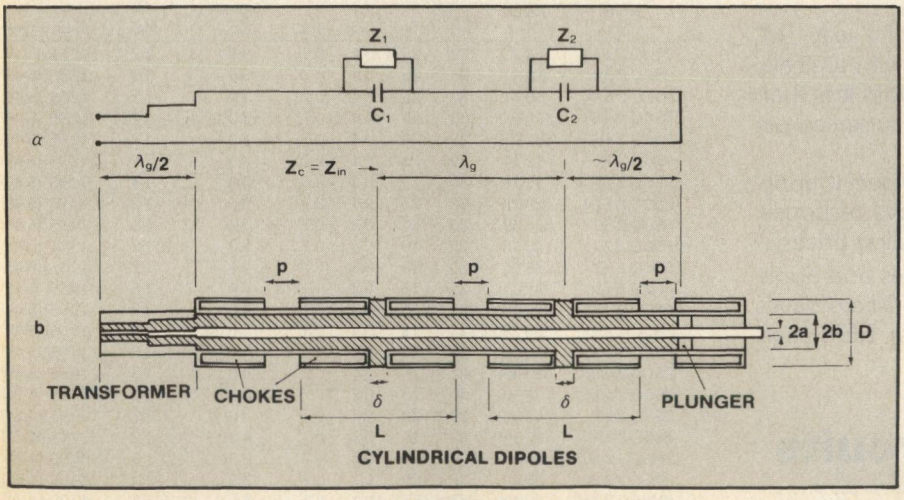

Fig.1 Two element omnidirectional antenna; A) equivalent circuit, B) antenna sketch.

—Array pattern

In our case, a beamwidth at -3 dB of nearly 36° being required in vertical plane, an array of two half-wave dipoles with equal amplitudes and phases has been investigated. His radiation pattern is:

$$E_\theta(\theta, \varphi) = \cos\left(\frac{\pi\, d \cos\theta}{\lambda}\right) \frac{\cos\left(\frac{\pi}{2}\cos\theta\right)}{\sin\theta} \quad (1)$$

while $E\varphi\ (\theta, \varphi) = 0$ in spherical coordinates with the vertical Z axis ($\theta = 0$) coincident with the array axis. In practice an array distance $d = 0.7\lambda$ has been chosen, with a theoretical beamwidth BW = 37.4°, in order to realize the antenna in a simple manner. In fact we have completely filled the feeding resonant coaxial line with teflon, a low loss-tangent material with a dielectric constant ($\varepsilon = 2.04$ measured) fit to make the slot centers at 0.7λ distance to coincide with the maxima of stationary waves inside the line.

—Impedance matching

The series fed collinear resonant array has an equivalence scheme constituted essentially by

[Continued on page 114]

a sequence of series impedances in parallel to coupling capacitances (Figure 1).

The radiating elements are 0.7 λ spaced in air, or equivalently 1 λ_g spaced inside the coaxial line, their impedances are Z_1 and Z_2 and neglecting coupling capacitances the total input impedance is

$$Z_{in} = Z_1 + Z_2 + jZ_c \tan \beta l \quad \left(\beta = \frac{2\pi}{\lambda g}\right) (2)$$

This impedance Z_{in} must be equal to the characteristic impedance Z_c of the teflon filled coaxial line for a perfect matching.

In our case we have equal half-wave dipoles as radiating elements and Z_1 and Z_2 are equal and pure resistive with a good approximation.

Quarter-wave chokes don't change these impedances. Also short circuit distance can be put simply to 1/2 λ_g, so that impedance matching, neglecting coupling capacitances, is achieved if Z_1 and Z_2 are Zc/2, because $Z_{in} = Z_1 + Z_2$ in this case. To ensure to same extent the stiffness of the antenna, suitable diameters have been chosen for the internal and external conductors of the coaxial line which feeds the dipoles. So its characteristic impedance has resulted to be $Z_c = 59.4\ \Omega$, a pure resistance, and a quarter-wave transformer has been added to pass from the $Z_o = 50\Omega$ of a standard feeding cable to this Z_c.

—Element design

The radiating element consists essentially of a cylindrical dipole fed by an annular slot cut on the external conductor of a coaxial line. The dipole impedance can be found on Jasik's Handbook and it agrees for a length to diameter L/D = 3.35 with the value $Z = 29.7\ \Omega$ we have obtained.

Further in the dipole impedance there is to consider the additional capacitance C due to slot edge coupling (Figure 1). Following the formulas reported by Chang[3] we have obtained a negligible C with a slot gap δ = 12 mm and a radii ratio b/a = 4.16. However in his article the thickness of the external cylindrical conductor is zero. In our case, in which the thickness adds to skirt parallel facing parts, a little bigger coupling capacitive reactance results from that portion of parallel plate radial waveguide between coaxial line and cylindrical dipole. To compensate this capacitance and some small reactances introduced by non ideal chokes (for construction simplicity their dielectric filling has been avoided), it has been useful to tune the plunger at the end of the array at a value a little different from $\lambda g/2$ to optimize the impedance matching experimentally.

It is remarkable that a very similar configuration to that described by[1] can be obtained putting the short circuit not at $\lambda g/2$ from the center of the last dipole but at the end of its gap of length δ. However in this case the short circuit would be at d/2 from the center of the last dipole and it would create a small reactance. Therefore this little mismatch, which can be calculated by (2), would insert a little difference in amplitude and phase of radiating dipoles if it is not compensated in some way. In our case we have found an unsatisfac-tory matching putting the short circuit in this position.

Experimental Results

Owing to the rotational symmetry of the antenna in the φ-coordinate we have obtained a perfect omnidirectional azimuthal pattern and a cross component $E\varphi = 0$ in the limits of measure sensitivity. A return loss below 20 dB has been measured in the band 1030 ÷ 1060 MHz.

The experimental and theoretical elevation radiation pattern at 1030 MHz with an array spacing of 0.7 λ is shown in Figure 2. The measured beamwidth at -3 dB is BW = 35°, against BW = 37.4° calculated by (1).

But, while the theoretical collinear array produces a symmetrical beam whose peak is at the horizon and has -16.5 dB of side-lobe level in vertical, our antenna tilts its beam about 9° above horizon and has no secondary lobes under it.

This difference is due to surface currents not completely stopped by the decoupling chokes and means that our antenna suffers

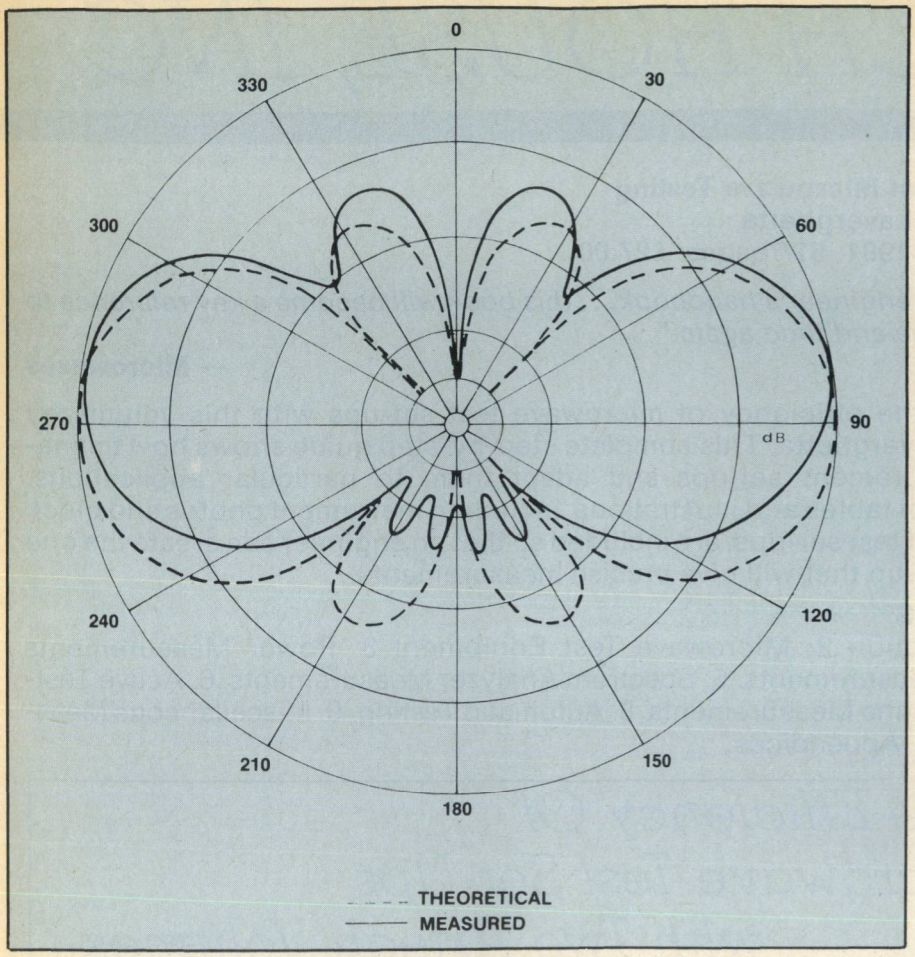

Fig. 2 Elevation radiation patterns.

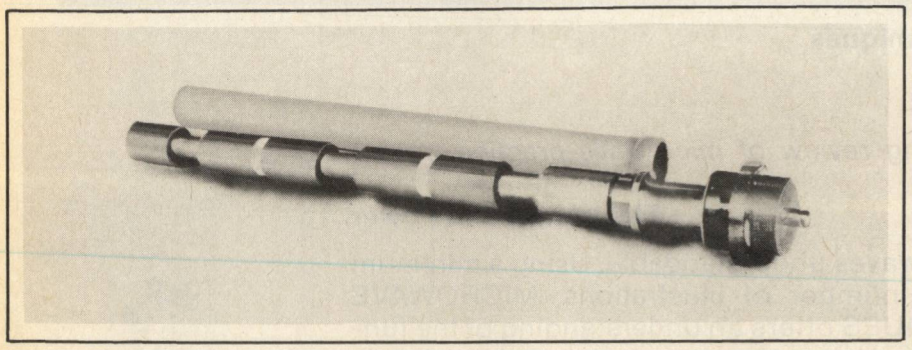

Fig. 3 The omnidirectional antenna.

ground reflection echoes less than the theoretical one.

The measured beamwidth BW = 35° implies a gain $G \simeq 5$ dB which has been obtained from[4]:

$$G \simeq 10 \log_{10} \frac{101}{BW - 0.0027\,(BW)^2} \qquad (3)$$

The antenna is shown in Figure 3 with its fiberglass cover for stiffness improvement and weather protection.

Acknowledgement

The author is grateful to B. Palumbo and F. Lomaglio for the helpful discussion and to F. Tregua for the experimental work.

REFERENCES

1. Jasik, H.: "Antenna Engineering Handbook" (Ch. 3 and 22), N.Y., McGraw Hill 1961.
2. Silver, S: "Microwave Antenna Theory and Design" (Ch. 8.2), N.Y., Dover 1965.
3. Chang, D.C.: "Equivalent Circuit Representation and Characteristics of a Radiating Cylinder Driven Through a Circumferential Slot", IEEE Trans., 1973, AP-21, Nov., pp 792-796.
4. McDonald, N.A.: "Approximate Relationship Between Directivity and Beamwidth for Broadside Collinear Arrays", IEEE TRANS, 1978, AP-26. ■

Technical Feature

Instantaneous Simultaneous Signal Detecting

James Tsui, Rudy Shaw
Wright-Patterson AFB, OH

James Cisar, Timothy Ratliff
Systems Research Laboratories, Inc.

Introduction

The Instantaneous Frequency Measurement (IFM) receiver is a special type of receiver which has been proposed for many Electronic Warfare (EW) applications. The receiver's basic frequency measurement technique consists of comparing the phase of a signal at the output of delay lines of known length. The receiver can only read one input signal at a time. If multiple signals arrive at the input of the receiver, the frequency reading might be erroneous. It is crucial for the processor to know if the frequency information might be erroneous. One approach is to have a detection circuit to sense the condition of simultaneous signals. This paper will present several simultaneous signal detection schemes for IFM receivers and their performance.

The operational principle of an IFM receiver can be explained as follows. A sinusoidal wave is split into two paths by a power divider, and one path is delayed by a constant time with respect to the other one. The phase delay between the two signals is frequency dependent. By measuring this phase delay, the frequency of the input signal can be derived. In a practical IFM receiver, the basic frequency measurement circuit is arranged as shown in Figure 1. The input signal is divided into two paths with one signal delayed. Both these signals are fed into a phase discriminator which has four outputs, and each one is followed by a crystal detector. The outputs of the detectors are connected to the inputs of two differential amplifiers. If the detectors are operating as square law devices, the outputs of the differential amplifiers can be expressed as sin $\omega\tau$ and cos $\omega\tau$ where ω is the input angular frequency and τ is the delay time. By measuring or digitizing the sin $\omega\tau$ and cos $\omega\tau$, the frequency can be read. A more detailed operational principle of IFM receiver can be found in references 1-3.

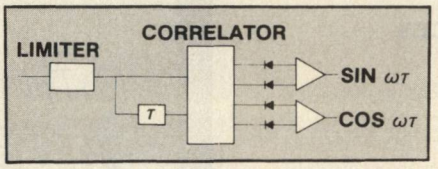

Fig. 1 Basic frequency measurement circuit in an IFM receiver.

Two Simultaneous Signal Conditions

In order to simplify the discussion of simultaneous signals, only two signals are considered. Basically there are two kinds of simultaneous signal conditions that can cause the receiver to generate erroneous frequency data. The first condition is when the leading edges of the two signals are time coincident (in general, they can be within 10 ns of each other). The second condition is that the signals are not time coincident, but the second signal arrives before the frequency of the first signal is properly encoded.

The time coincident case has been analyzed and evaluated by many different IFM receiver manufacturers and users. The general comments are that when the power levels of the two signals differ by more than 6 dB, the receiver will generate a negligible percent of erroneous data. It should be emphasized that even with two signals of the same amplitude (the worst case for a type 1 condition), the erroneous frequency data generated will be less than 25 percent. Therefore, this simultaneous signal condition is arguably not very serious, since the chance of having two signals of approximately the same amplitude and also time coincident is very small.

In the second simultaneous signal condition, if the first signal is stronger than the second one, the receiver generates very little erroneous frequency information. However, if the first signal is weaker than the second one, the receiver may generate as high as 80 percent erroneous data. The results of extensive testing of this condition have been published in reference 4. The reason for such a high erroneous data rate can be explained as follows. The first signal will trigger the frequency measurement circuit, and the second signal will cause a transient state

at the outputs of the comparators where the sin $\omega\tau$ and cos $\omega\tau$ are generated. This is shown in Figure 1. When the frequency measurement circuit takes a frequency sample during this transient state, a high probability of erroneous data will be generated.

Analog Simultaneous Signal Detection Circuits

The most commonly proposed simultaneous signal detection circuit consists of a mixer used in a homodyne configuration followed by a bandpass filter of proper bandwidth. At the output of the filter, a detector and comparator are used as shown in Figure 2. If one signal arrives at the mixer, all harmonics are generated by this single input signal. These harmonics will be outside the bandwidth of the filter. Thus, there will be no output from the detector/comparator circuit. When two or more signals arrive at the mixer, harmonics related to the difference frequency of the input signals will be generated. These harmonics pass the filter and are detected and produce an output at the comparator.

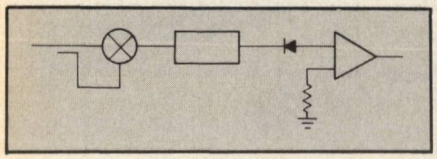

Fig. 2 Detecting circuit using a mixer followed by a bandpass filter.

This detection circuit is sensitive to simultaneous signals which have comparable amplitudes. When the amplitudes of input signals are far apart (i.e., beyond 6 dB), the amplitudes of harmonics generated relative to the difference frequency are rather low. Therefore, this detection circuit is useful in detecting the first kind of simultaneous signals previously mentioned, but relatively insensitive to the second type of simultaneous signals.

Observing the sin $\omega\tau$/cos $\omega\tau$ from the outputs of the differential amplifiers under the second kind of simultaneous signal condition, shows that there is usually a dip in the video output when simultaneous signals are present. One of the typical outputs is shown in Figure 3. Figure 3 shows the results of a weak signal followed by a strong one. Note in this figure that the video output changes from the voltage corresponding to the weak signal to the voltage corresponding to the strong one, and when this occurs, there is a dip between the two states. The cause of this dip is ascribed to the mixing effect in the limiting amplifier usually installed in an IFM receiver before the video detector. The limiting amplifier is a non-linear device and, when two or more signals are present, harmonics are generated. These harmonics take the energy from the desired frequency; as a result the corresponding video voltage decreases. As previously mentioned, most of the harmonics are generated when the two input signals are approximately at the same level. This situation occurs on the leading edge of the second signal. When the amplitude at the leading edge of the second pulse is rising, there is an instant at which the two signals have approximately the same power levels, producing the dip in the video voltage.

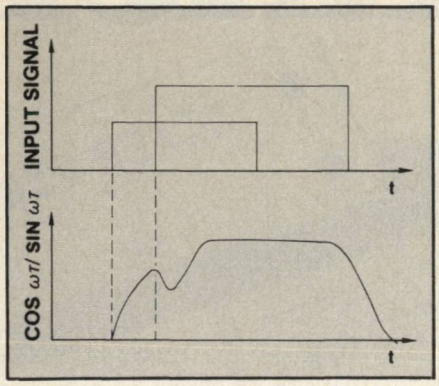

Fig. 3 A weak signal followed by a strong one and their corresponding output.

Two approaches were tried to detect the dip in the video output. Both have had some success. The first method is to sample and hold on the video output and compare with the rest of the pulse[5] as shown in Figure 4. The second method is to separate the video signals into two paths, attenuate and delay one of the signals, and compare the amplitude. When there are simultaneous signals, the result is as shown in Figure 5, where the peak of the delayed pulse is higher than the undelayed one.

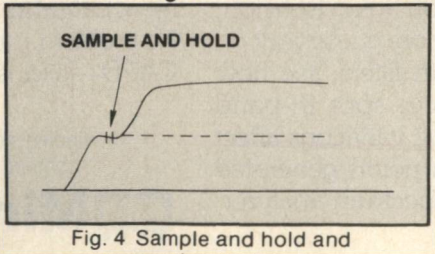

Fig. 4 Sample and hold and comparison scheme.

The shortcoming of both approaches is that if the detection circuit is adjusted for minimum false alarm, its sensitivity for detecting simultaneous pulses also degrades. For this consideration false alarm is defined as the indication of simultaneous signals when there is only one input signal. This difficulty arises from the fact that under varying pulse overlap conditions, the leading edge on the video pulse changes. It is difficult to design a circuit which detects all conditions. Both circuits were built and tested in the laboratory. When the circuits were adjusted to generate no false alarm over the entire frequency and dynamic range of the receiver, preliminary experiments have shown that the detection circuits could report about 5 to 50 percent of the pulse overlap under various input conditions.

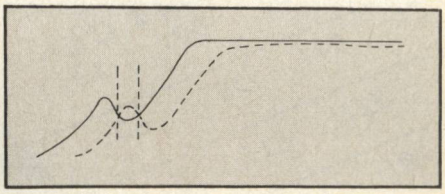

Fig. 5 Delay and comparison scheme.

Digital Simultaneous Signal Detection Scheme

This detection scheme is based on the identity $\sin^2\omega\tau + \cos^2\omega\tau = 1$. Taking the sum of the square of both the sin $\omega\tau$ and cos $\omega\tau$ outputs, a constant output level is maintained. If any output level is lower than 1, it indicates a simultaneous signal condition. This detection circuit should be applicable to both of the simultaneous signal conditions mentioned in Section II. The sum and squaring of the two video outputs can be accomplished through A/D converters and digital manipulations. However, the problem is more complex. Although there is usually a limiting amplifier in an IFM receiver, the sum of the squared

[Continued on page 122]

[From page 119]

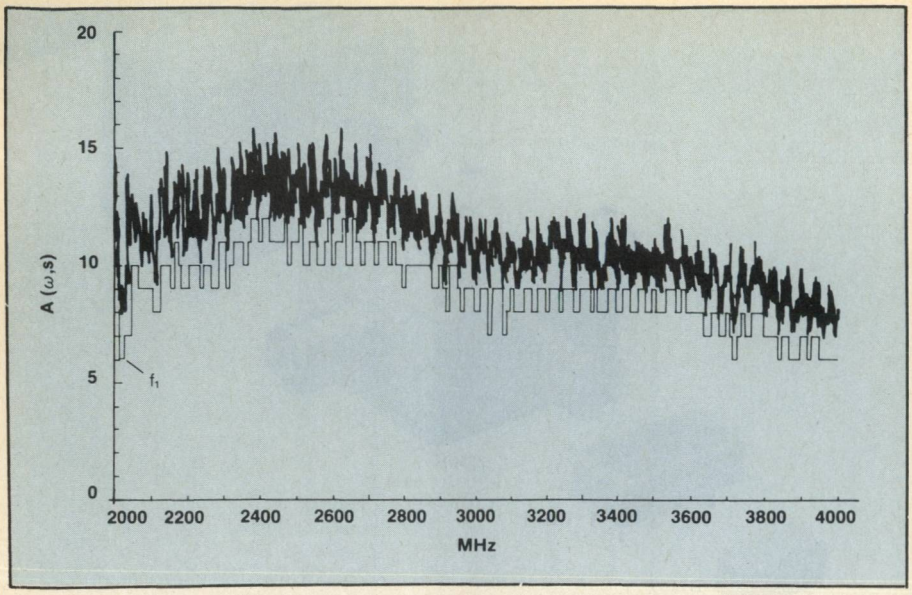

Fig. 6 Amplitude A (ω, s) as a function of frequency (ω).

video outputs is frequency dependent. In other words, the outputs from the differential comparators are A (ω, s) sin $\omega\tau$ and A (ω, s) cos $\omega\tau$ rather than simply sin $\omega\tau$ and cos $\omega\tau$. The symbol A (ω, s) means the amplitude depends on the input frequency ω and its signal strength s. The amplitude change of the video signal is due to the amplitude variation of frequency response of the RF components used in the receiver. A typical $(A(\omega, s)\sin^2\omega\tau + A^2(\omega, s)\cos^2\omega\tau)^{1/2} \cong A(\omega, s)$ curve is shown in Figure 6. In Figure 6, a constant input power level is used. If the input signal level is changed, the general shape of the curve shifts slightly.

To implement this frequency dependent correction, read only memory (ROM) is used to store threshold values which are slightly lower than the lowest A (ω, s) existing within a bin. These threshold levels are accessed from the ROM by the receiver's reported frequency. Since the threshold does not vary rapidly with ω, not all the frequency bits are needed. For example, an IFM receiver with 11 bits of frequency information may only need 8 bits or less in the threshold ROM. A/D converters followed by a ROM to implement the function $\sqrt{a^2 + b^2}$ are used to generate the measured value of A (ω, s). Sampling is coincident with the receiver's sample time. The measured A (ω, s) is compared to the threshold, and when it is below the threshold, a flag is set to indicate the simultaneous signal condition.

The basic circuit is shown in Figure 7. The circuit detects the simultaneous signals 70 to 95 percent of the time. As expected, this detection circuit misses the pulse overlap condition for which there is no significant dip in the video output. The other condition that the circuit fails to detect occurs when the erroneous frequency reading is at f_1 where the threshold is low. The measured A (ω, s) may be higher than the threshold under this condition.

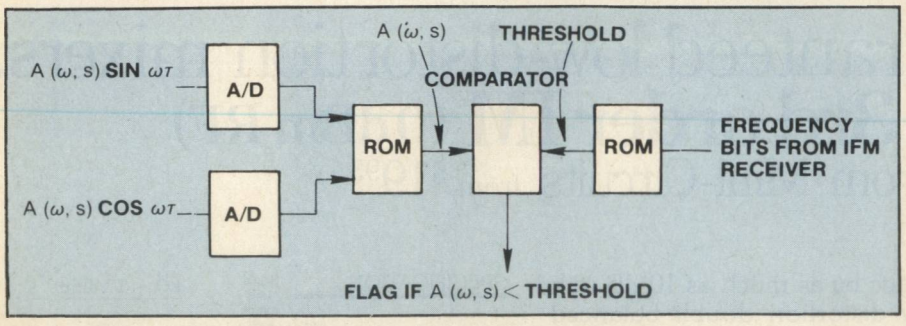

Fig. 7 Digital simultaneous signal detection scheme.

It should be emphasized here that when the simultaneous circuit detects the existence of pulse overlap, the frequency reading from the IFM receiver may still be correct.

Re-Sampling the Frequency Information

When a weak signal is followed by a strong signal, if one can delay the frequency measurement time gate, the frequency of the strong signal will be obtained. The digital simultaneous signal detection circuit will detect the existence of simultaneous signals at the time a frequency sample is made, for which condition the sampling gate can be delayed a short time (e.g., approximately 100 ns) and another measurement made. If the overlap condition is of the second kind as described in Section II, the chance of obtaining correct frequency information is very high. There are many ways by which this idea can be implemented. A repetitive sampling scheme can also be used. If the trailing edges of the overlapping pulses are not time coincident, the chance of obtaining the correct frequency information is very high. This capability would greatly improve the performance of an IFM receiver.

A re-sampling circuit was built and successfully tested in the laboratory. Preliminary data showed that the percent of erroneous frequency measurements can be reduced from 50-60 percent to less than 10 percent.

REFERENCES

1. Myers, G.A., Cumming, R.C., "Theoretical response of a polar-display instantaneous-frequency meter," *IEEE Trans. Instrumentation and Measurement*, Vol. IM-20, pp. 38-48, February 1971.

2. Heaton, D., "The systems engineer's primer on IFM receivers," *Microwave Journal*, p. 71, February 1980.

3. Gourse, S.J., Worrell, E.A., "Wide-band IFM flyable brassboard," *Final Engineering Report*, Litton Amecom, College Park, Maryland, November 1974.

4. Shaw, R.L., Tsui, J.B.Y., "IFM receiver test and evaluation," *Technical Report AFAL-TR-79-1049*, Air Force Avionics Laboratory, Wright-Patterson Air Force Base, April 1979.

5. Tsui, J.B.Y., Shaw, R.L., "Simultaneous Signal Detection Capability for Instantaneous Frequency Measurement (IFM) Receivers," Patent Case #13741. ■

Technical Note

Universal Attenuation Curves for Rectangular and Circular Waveguide

A.J. Baden Fuller
Department of Engineering
University of Leicester
Leicester, England

Abstract

Graphs give the value of attenuation constant against a normalized frequency, so that the characteristic free-space wavelength is measured in units of the broad dimension of rectangular waveguide or the diameter of circular waveguide. The results can then be scaled to any size of waveguide. One graph gives the results for the first fourteen modes in rectangular waveguide and the other those for the first fifteen modes in circular waveguide.

Introduction

Two graphs give the value of attenuation constant in rectangular or circular waveguide calculated from theoretical expressions. The frequency axis is normalized so that the characteristic free-space wavelength is measured in units of the broad dimension of rectangular waveguide or the diameter of circular waveguide. The results can then be scaled to any size of waveguide. The theoretical expressions and their derivation are given in reference 1, together with small scale reproduction of these Universal Attenuation curves. It is felt that a larger-scale version of the central part of the same curves will be a useful design aid. The theoretical expressions for attenuation are derived from the low-loss approximation that calculates the propagating conditions assuming the attenuation to be zero and then uses the resultant field values to calculate a theoretical attenuation value. So these results are not valid for large values of attenuation, and make no allowance for any change in phase constant or any mode coupling due to the finite conductivity. The theoretical expressions which are used to calculate the curves are reproduced in the final section of this note.

Rectangular Waveguide

The results calculated for the first fourteen modes in rectangular waveguide are given in Figure 1. They are scaled in terms of the broad dimension "a" of the waveguide for waveguides having a 2:1 aspect ratio, i.e. a=2b. The horizontal axis is λ_o/a, which is dimensionless, or the equivalent frequency is fa, which has the units m/s. The attenuation then comes out to be $\alpha a^{3/2}$. These slightly awkward units occur because the skin depth expression contains the square root of the frequency. A numerical conversion is used so that the attenuation constant is given in dB/m and the vertical axis is calibrated in $dBm^{1/2}$. The attenuation constant is calculated for drawn copper waveguide assuming a conductivity of 4.00×10^7 S/m. This figure is known to be a good approximation at about 10 GH_z, and a round number was chosen for the conductivity of copper to aid scaling. For other waveguide materials, the attenuation constant can be scaled according to the square root of the ratio of the conductivities.

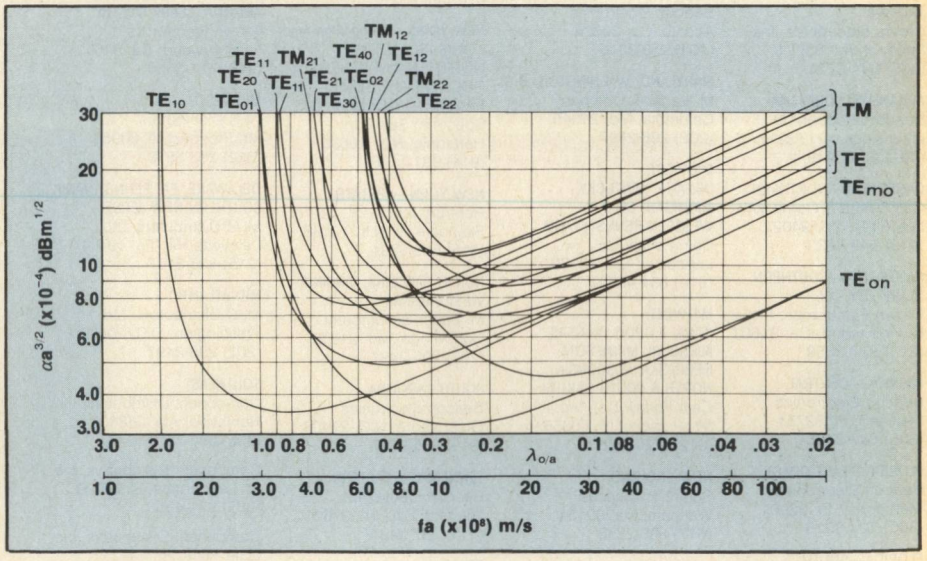

Fig. 1 Values of attenuation constant for the first few modes in rectangular waveguide, for 2:1 aspect ratio, width a, plotted against normalized wavelength.

It will be noticed that although the dominant TE_{10}-mode is a low-loss mode, the TE_{01}-mode has the lowest value of attenuation constant. Further, because of the scaling properties of the curves, if two

sizes of waveguide are chosen so that the TE_{10} -mode and the TE_{01} -mode have the same cut-off frequency, then the TE_{01} -mode in the larger size of waveguide will have a lower value of attenuation constant at any particular frequency.

modes in large size circular waveguide. These low attenuations may help the designer choose the best mode of operation of high Q resonant cavities, although the resonating fields are not identical with the propagating fields used to calculate these curves.

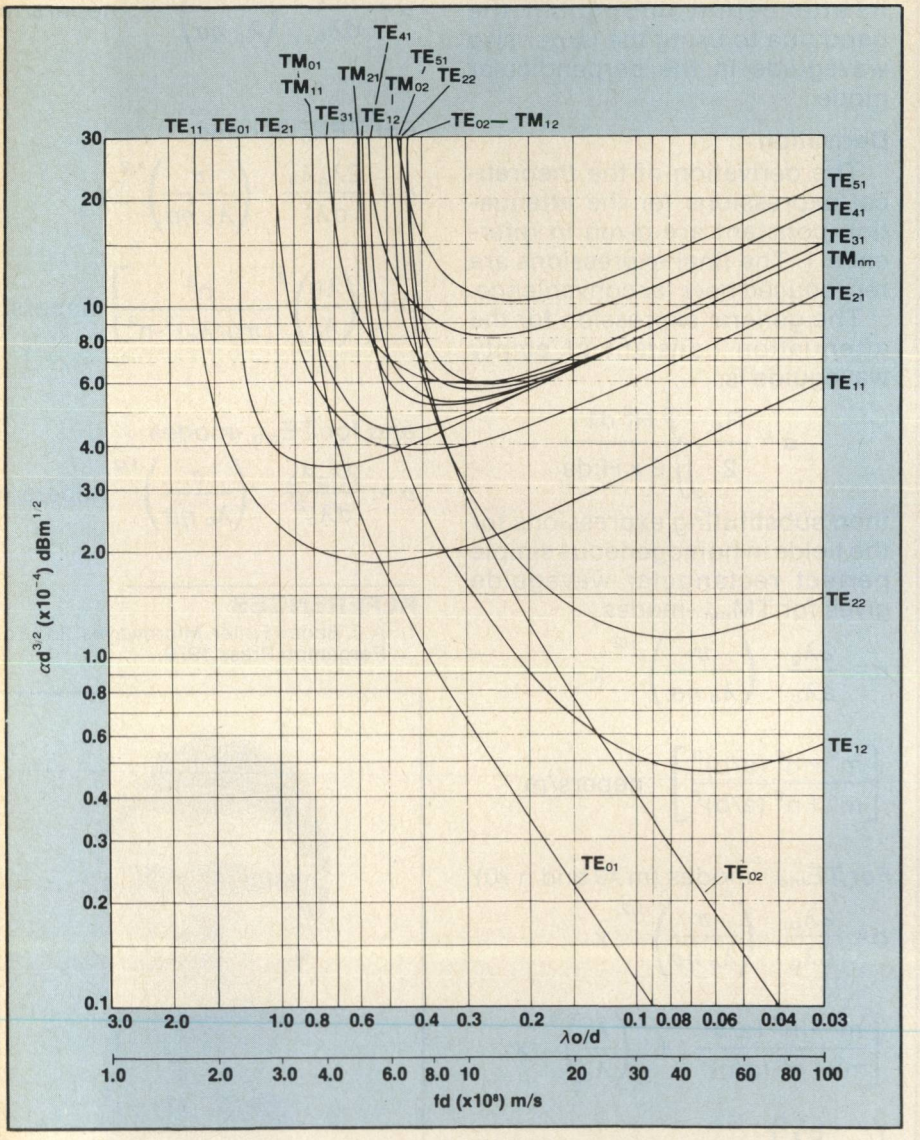

Fig. 2 Values of attenuation constant for the first few modes in circular waveguide, of diameter d, plotted against normalized wavelength.

Circular Waveguide

The attenuation calculated for the first fifteen modes in circular waveguide is given in Figure 2. The horizontal axis is scaled, similarly to the results in Figure 1, in terms of the inside diameter d of the waveguide. The horizontal axis is λ_o/d and the attenuation axis is $\alpha d^{3/2}$. Again the conductivity of drawn copper waveguide is taken to be 4.00×10^7 S/m. These curves clearly shown the low attenuation of some of the higher order TE-

Example

As an example of the use of the curves, we will find the attenuation at 18 GHz for the dominant mode in WR 62 and for the same frequency wave in the TE_{01}-mode in WR 159. At 18 GHz, $\lambda_o = 1.67$ cm.

1. **For WR 62**, a = 0.622 in = 1.58 cm.
   Therefore, $\lambda_o/a = 1.055$.
   From Figure 1 from the TE_{10} - curve, $\alpha a^{3/2} = 3.7 \times 10^{-4}$ dB $m^{1/2}$.
   Therefore, $\alpha = 0.186$ dB/m.

[Continued on page 126]

[From page 125] **ATTENUATION CURVES**

2. **For WR 159**, a = 1.590 in = 4.04 cm.
Therefore, $\lambda_o/a = 0.4125$
From Figure 1 from the TE_{01} - curve, $\alpha a^{3/2} \approx 3.7 \times 10^{-4}$ dB $m^{1/2}$.
Therefore, $\alpha = 0.0456$ dB/m.

Further applications show that there is a similar 4:1 improvement in attenuation throughout the band due to using the larger size waveguide in the perpendicular mode.

Derivation

The derivation of the theoretical expressions for the attenuation constant are given in reference 1. The final expressions are reproduced here for convenience.

The general expression for the attenuation constant of empty waveguide is:

$$\alpha = \frac{R_s}{2} \frac{\oint H_t^2 \, d1}{\iint \underline{E} \times \underline{H} \cdot d\underline{a}}$$

then substituting expressions for the fields in homogeneous simple perfect rectangular waveguide gives for TM_{mn} -modes

$$\alpha = \frac{2\lambda_g}{a\lambda_o} \left(\frac{\pi}{\lambda_o \eta \sigma}\right)^{1/2} \times \left[\frac{m^2 + n^2 (a/b)^3}{m^2 + n^2 (a/b)^2}\right] \text{ nepers/m}$$

For TE_{mm} -modes ($m \neq 0$ and $n \neq 0$)

$$\alpha = \frac{2\lambda_o}{b\lambda_g} \left(\frac{\pi}{\lambda_o \eta \sigma}\right)^{1/2} \times \left[\frac{m^2 + n^2 (a/b)}{m^2 + n^2 (a/b)^2} + \left(\frac{\lambda_g}{\lambda_c}\right)^2 \times \left(1 + \frac{b}{a}\right)\right] \text{ nepers/m}$$

For TE_{mo} -modes

$$\alpha = \frac{\lambda_o}{b\lambda_g} \left(\frac{\pi}{\lambda_o \eta \sigma}\right)^{1/2} \times \left[1 + \left(\frac{\lambda_g}{\lambda_c}\right)^2 \left(1 + 2\,\frac{b}{a}\right)\right] \text{ nepers/m}$$

For TE_{on} -modes

$$\alpha = \frac{\lambda_o}{a\lambda_g} \left(\frac{\pi}{\lambda_o \eta \sigma}\right)^{1/2} \times \left[1 + \left(\frac{\lambda_g}{\lambda_c}\right)^2 \left(2\,\frac{a}{b} + 1\right)\right] \text{ nepers/m}$$

For circular waveguide of diameter d for TM-modes

$$\alpha = \frac{2\lambda_g}{d\lambda_o} \left(\frac{\pi}{\lambda_o \eta \sigma}\right)^{1/2} \text{ nepers/m}$$

For TE_{nm} -modes

$$\alpha = \frac{2\lambda_g\lambda_o}{d\lambda_c^2} \left(\frac{\pi}{\lambda_o \eta \sigma}\right)^{1/2} \times \left[1 + \left(\frac{\lambda c}{\lambda_o}\right)^2 \frac{n^2}{(\pi d/\lambda_c)^2 - n^2}\right] \text{ nepers/m}$$

and for TE_{om} -modes

$$\alpha = \frac{2\lambda_g\lambda_o}{d\lambda_c^2} \left(\frac{\pi}{\lambda_o \eta \sigma}\right)^{1/2} \text{ nepers/m}$$

REFERENCES

1. A.J. Baden Fuller. Microwaves. 2nd Ed. Pergamon Press 1979.

John Baden Fuller, *obtained his MA with first class honours in Engineering from Cambridge University in 1955. Then he worked with A.E.I., Military Radar division designing microwave ferrite devices until 1964. He spent one year as a lecturer at Leicester College of Technology. Since then he has been a lecturer in electronics in the Engineering Department of Leicester University specializing in field theory and microwaves. He has written a textbook on Microwaves and two on Engineering Field Theory. Mr. Baden Fuller is a member of I.E.E.* ■

Quick Microwave Field Mapping for Large Antennas

G. Collignon, Y. Michel, F. Robin, J. Saint
Societe d'Etude du Radant

J.C. Bolomey
Groupe d'Electromagnetisme
Ecole Superieure d'Electricite

Introduction

In many applications, such as antenna near field probing or microwave imaging, the main problem consists in the measurement of electromagnetic field distributions over large areas. Typically, the dimensions of these areas are in the order of 10 to 100 wavelengths. Furthermore the sampling interval is only a part of a wavelength in such a way that the number of measurement points is very high, usually a few thousand.

In most of the situations the probing accuracy is of prime importance, in some others, the probing speed is more important.

This is particularly the case for antenna adjustments, dynamic test of phased arrays or real time imaging. This paper deals with the measurement duration and demonstrates fast electromagnetic field recording by using the modulated scattering technique (M.S.T.). First, the major features of classical solutions are reviewed. These solutions are based mainly on mechanical scan and on an array of probes. Next, the principle of the M.S.T. is given and its particular use for fast probing is considered. The third part is devoted to the description of an S-band experimental set-up and to the discussion of the obtained results. Special attention is given to the measurement speed and accuracy.

Classical Solutions for Near Field Probing

The simplest and customary way for recording microwave field distributions is to move a probe over the area to be investigated. However, with such a mechanical scan, the measurement time is limited ultimately by the finite speed of the probe. Even for speeds of about a few centimeters per second, typical antenna measurements take hours.

Probe movement can be avoided by using arrays of fixed probes (figure 1). The shortest measurement time, of course, would be provided by parallel arrangement in which each probe has its own receiver. Probably the solution of the future, with the development of monolithic microwave integrated circuits, will allow individual receiver insertion on sur-faces as small as a few square millimeters. Meanwhile, the measurement time is reduced to the acquisition time of the receiver and then depends on the required dynamic range.

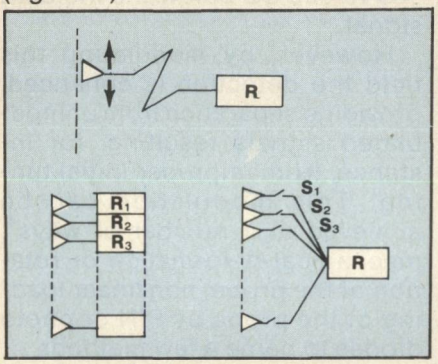

Fig. 1 Probe arrays: a) parallel arrangement, b) series arrangement.

In the series arrangement, a microwave multiplexer (switching network) is used for connecting the probes to a single receiver or at least to a reduced number of receivers. As shown in figure 1 b, the multiplexer can be realized by means of switches. Thus, the measurement time is mainly limited by the switching time, which in turn depends on the device used for switching (electromechanical or electronic). Table 1 gives approximate speeds for these classical solutions. Clearly, a multiple probe array provides a great reduction of the measurement time as compared to the mechanical scan solution.

Real time or quasireal time measurement mandates a probe array. But the design and the making of such arrays is both complex and expensive, due to the large number of elements and their high packing density at the wavelength scale. Another complexity is the multiplexer, which contributes particularly to a limitation in the

TABLE I
COMPARISON OF MEASUREMENT DURATION FOR VARIOUS METHODS

PROBING TECHNIQUE		MEASUREMENT DURATION
Mechanical Scanning	v = 5 cm/s	40 min.
Probes Array	Electromech. switch τ = 10 ms	48 s
	Electronic switch τ = 10 μs	<0.2 s
	M.S.T. .5 ms/pt	2.4 s

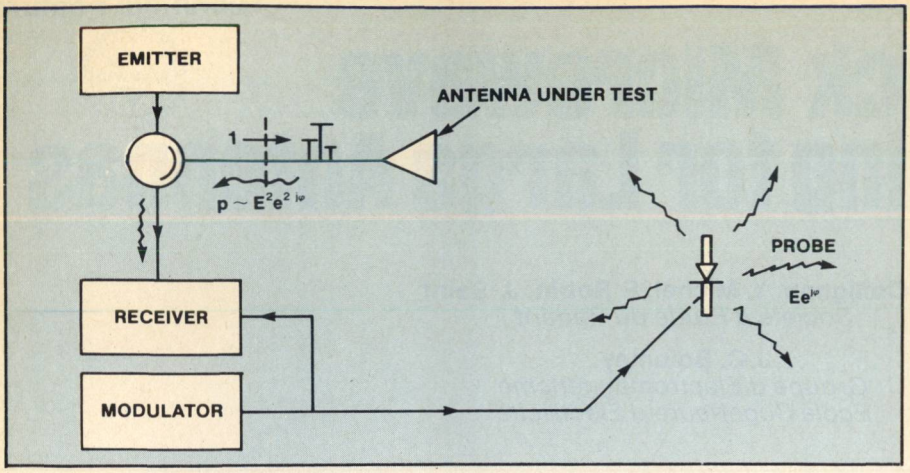

Fig. 2 Principle of the modulated scattering technique.

measurement accuracy, because of parasitic coupling between adjacent probes or because of the perturbation of the field to be measured by the array. Accordingly it is not surprising that the literature is not very rich in examples of arrays developed for near field measurement purposes. As will be seen, some of these difficulties are obviated by the MST.

The Modulated Scattering Technique (M.S.T.)

— Principle

The MST, initiated by Cullen and Richmond[1,2] in 1955, resembles a free space perturbation technique. In classical methods, the field to be measured is deduced from the signal delivered by the probe to its load, the receiver. In MST it is the field scattered by the probe which is measured. The measurement is usually done by the antenna under test itself, but it could be done by an ancillary antenna. In the first case, the antenna under test is connected to the source and to the receiver by means of a circulator (Figure 2). In the absence of the probe, the tuner is adjusted to cancel all signals to the receiver. The introduction of the probe destroys the previous adjustment. By reciprocity is follows that the signal reaching the receiver is simply related to the field at the probe location. If $A\,e^{j\varphi}$ is the complex component of the field to which the probe is sensitive, the signal at the receiver is proportional to $A^2\,e^{2j\varphi}$.

Presumably, there need be no microwave connection between the probe and the receiver. The perturbation introduced by the probe is measured directly. But the method has poor sensitivity due to the weakness of the scattered fields. Typically, the equivalent reflection coefficient is 100 to 120 dB below the incident signal.

However, by modulating this field the detection is enhanced, providing separation from unmodulated signals resulting, for instance, from improper initial tuning. This modulation can be achieved in a number of ways[4]: mechanical deformation or rotation of the probe, non linear loading of the probe by PIN or photo diodes to name a few methods ... Non linear loading seems to provide a good compromise between the ease of delivering the modulation signal, the perturbation introduced by the probe and the modulation efficiency. Even using a modulated laser beam could provide a perturbation free solution. But we have found that applying the modulation signal to PIN diodes by means of highly resistive leads proves to be a good and practical solution. The PIN diodes form a part of the array antenna to be measured in the example to be described[7].

— Radant Grids

Field probing over large areas can be achieved by assembling loaded dipoles. The diodes of the different dipoles have to be sequentially modulated according to a suitable addressing. The signal measured by the receiver during the corresponding time provides the amplitude-phase distribution of the field at the probes locations.

RADANT grids[5,7], consisting of an alignment of dipoles and continuous wires, constitute an interesting solution (Figure 3). Continuous wires can be used for carrying the modulation; furthermore they also contribute to the array matching when all the diodes are in the *off* state. In this state,

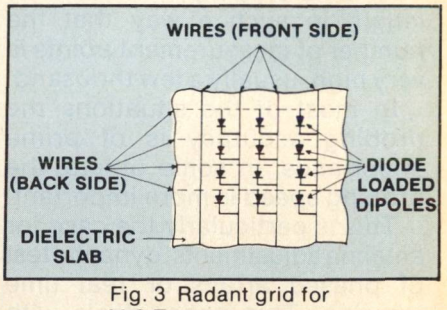

Fig. 3 Radant grid for M.S.T. measurements.

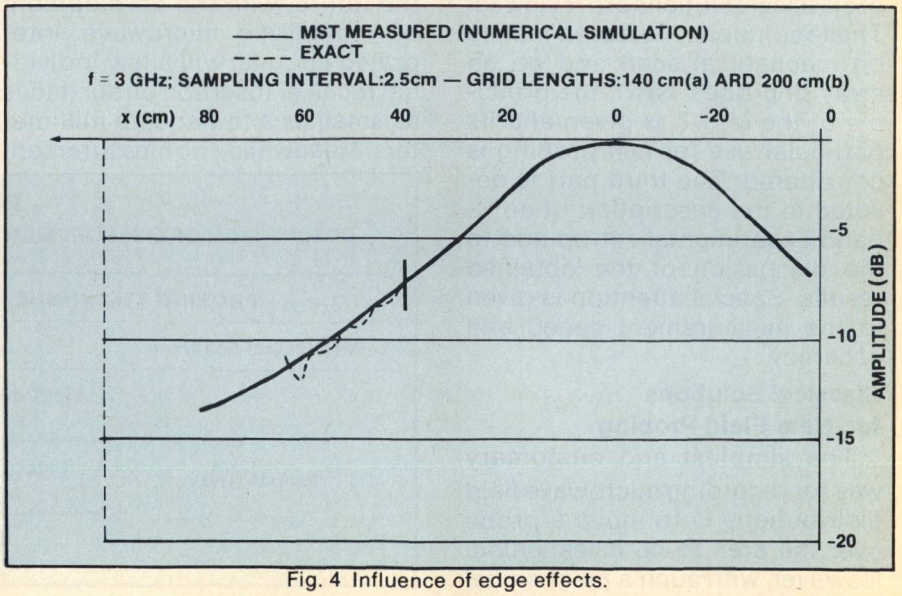

Fig. 4 Influence of edge effects.

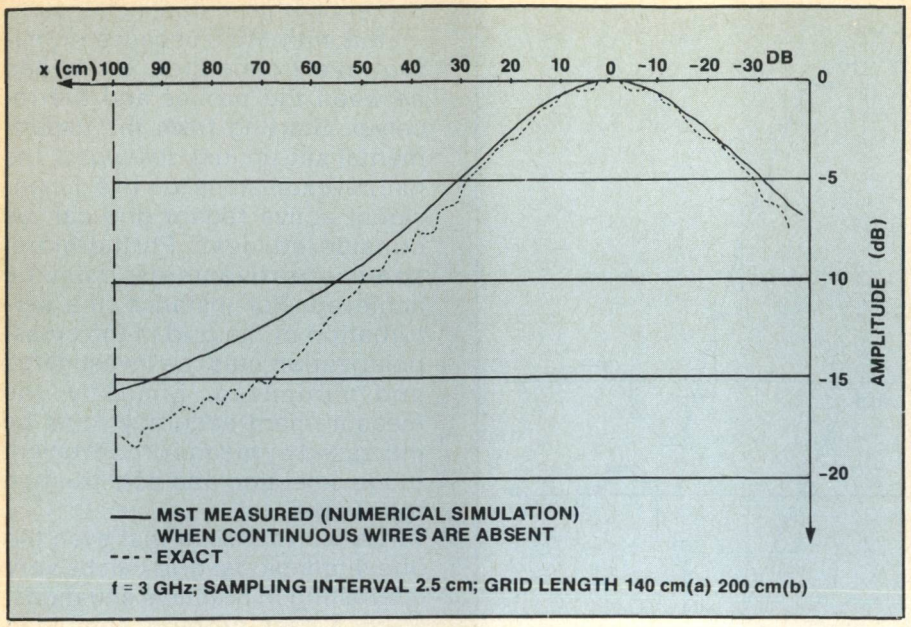

Fig. 5 Influence of matching the grid.

the grid is transparent and nonreflecting; the reflection of the array is minimized. The match is obtained by combining the capacitive effect of the loaded dipoles with the inductive effect of the wires. Accordingly, if a given diode is in the *on* state, then its proximate area behaves as a small reflecting screen. Modulating this diode at a low frequency rate results in a modulated signal at the receiver with the same frequency.

The array design can be performed with the aid of already available numerical codes[6]. Assuming grids of infinite extent and plane wave illumination, these codes allow the determination of the geometrical characteristics of the grid, for given diodes, in order to achieve the matching in the *off* state of the diodes. Other two-dimensional numerical simulations, including finite grids and arbitrary illumination, likewise have demonstrated the feasibility of the approach. In particular, the effect of the coupling between adjacent dipoles has been considered. This effect does not appear too critical, at least for well matched arrays. More critical are edge effects due to the finite length of the array. The array must not be interrupted in regions of high field. Tapers larger than 10 dB are suitable. Both matching and edge influences are illustrated in figures 4 and 5.

S-Band Experimental Set Up

— Description

An experimental array set up has been designed and built for operation from 2.8 to 3.2 GHz. The probe array is a 3 m x 1 m rectangle. Actually, only one line of 115 dipoles has been loaded by diodes. The other dipoles simulate an *off* state diode loading. The VSWR of the array is less than 1.5 for normal incidence in the frequency band. The modulation frequency is 50 kHz. The source delivers a one watt signal. The receiver has a sensitivity of about -140 dBm at 3 GHz. A carefully tuned and stable initial zero is obtained by reinjecting an amplitude-phase controlled part of the emitted signal. Figure 6 shows a schematic view of the experimental set-up.

— Results

The following results are relevant to two antennas. The first one is a pyramidal horn with a rectangular aperture of 33 x 24 cm. The probe array is located at 30 cm from the horn aperture. The real and imaginary part of the field are plotted on figure 7. The measured results are compared to those

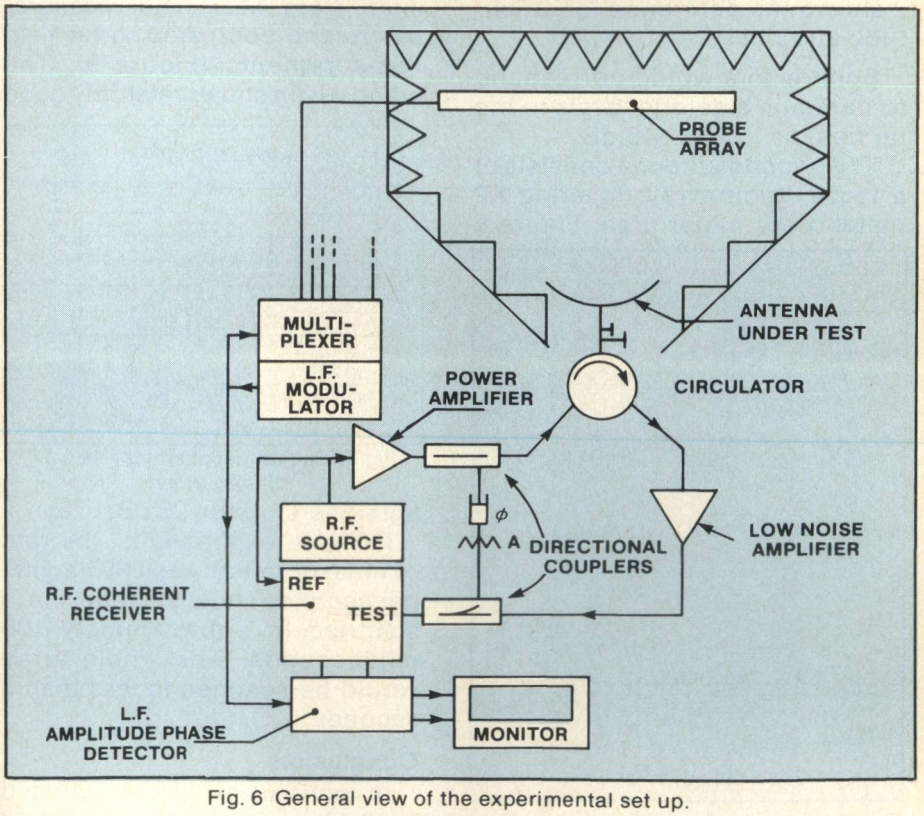

Fig. 6 General view of the experimental set up.

TABLE II

	RELATIVE AMPLITUDE %	PHASE DEGREES
Max error	6	4
Root mean sq. error	3	2.2

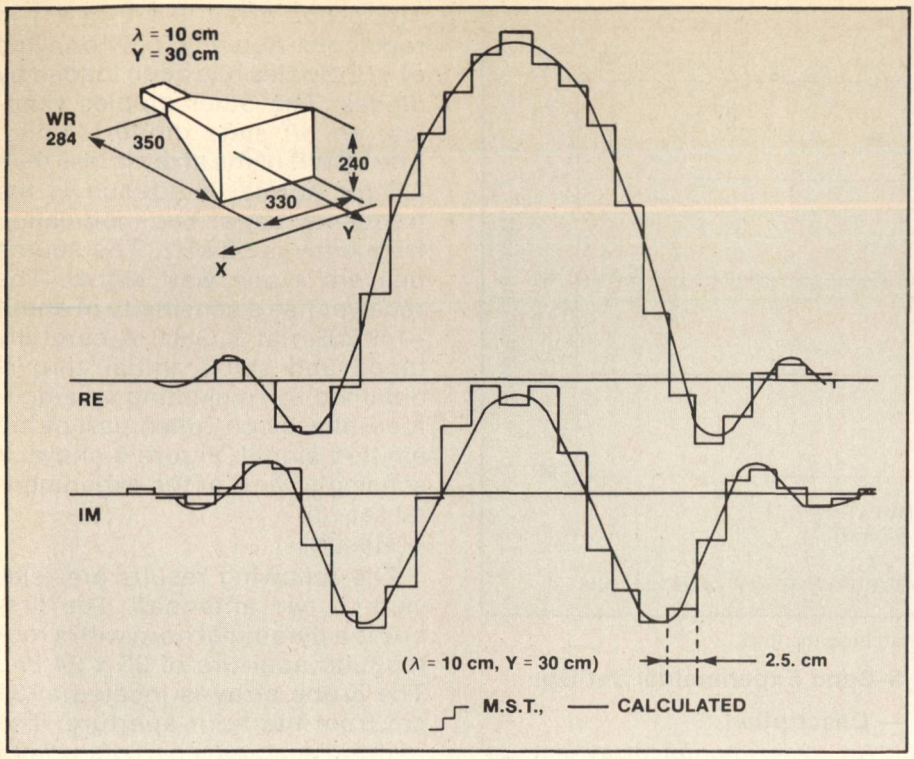

Fig. 7. Near field probing of a rectangular horn.

which have been calculated. Table 2 shows the difference for amplitude and phase.

Such errors would correspond to parasitic sidelobe levels in the far field as low as -46 dB.

The second antenna consists of a 16 x 4 dipole array, covering 1.2 meter x 0.4 meter area. Figure 8

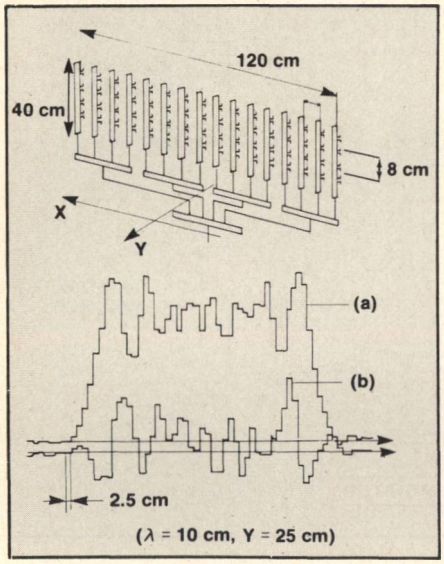

Fig. 8 Near field probing of a 16 x 4 dipoles array.

shows the real and imaginary parts of the field. The measurement have been done at 25 cm from the array plane. Assuming the separability of the near field distribution, the radiation pattern in the azimuthal plane has been calculated from near field measurements and compared to far field measurements (Figure 9). The comparison shows relatively good

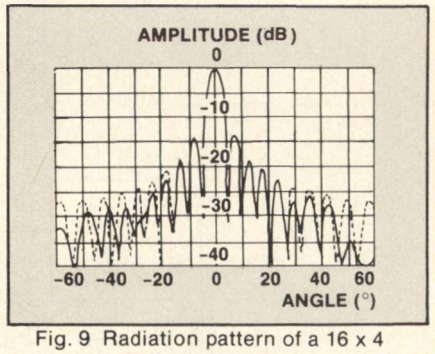

Fig. 9 Radiation pattern of a 16 x 4 dipoles array.

agreement up to -25 dB.

In these experiments, the rate of measurement was 2000 points per second. Thus, the total line is scanned in approximately 100 milliseconds. The whole array would be scanned in less than 3 seconds.

Conclusion

In conclusion the modulated scattering technique is an efficient way to probe at a rate of 2000 measurement points per second. Quasi real time operation is achieved for a few thousand points. This rate is of the order of magnitude of classical probe arrays using a microwave multiplexer but this multiplexer is eliminated with MST because no microwave connection is needed between the probes and the receiver. Starting from the experimental set-up just described, the natural extensions to a two dimensional active radant grid can be considered next. Furthermore, some improvements must be achieved. For instance, the perturbation of the grid in the cross-polarization must be investigated and minimized. Similarly, the measurement accuracy must be increased by means of convenient diode selection and construction tolerances.

It is worth noting that even the one dimensional grid can be very interesting in practical situations. Such a fast probing combined with a one axis antenna rotation provides an efficient means for measurements over cylinders. The simultaneous measurement of both orthogonal polarizations does not pose too many difficulties.

What has been said for near field probing can be extended easily to other problems such as imaging. There is no doubt that quasi real time facilities will be used more frequently in this hitherto explored domain of microwave imaging which covers a large number of applications including active biomedical imaging, non destructive testing, and civil engineering.

REFERENCES

1. Callen A.L., Parr J.C., "A new perturbation method for measuring microwave fields in free-space," Proc. IEE, vol 102, p. 836, 1955
2. Richmond J.H., "A modulated scattering technique for measurement of field distribution," IRE Trans, MTT 3, pp 13-17, 1955.
3. King R.J., "Microwave homodyne systems," Peter Peregrines Ltd, 1977.
4. Bolomey J.C., "La methode de diffusion modulee: une approche au releve des cartes de champs micro-ondes en temps reels, Onde electronique, Vol 62 n°5 pp 73-78, May 1982.
5. Chekroun C. Herrick D, Michel Y., Pauchard R, Vidal P., "Radant: New method of electronic scanning," *Microwave Journal* Vol 24 n° 2, pp 45-53, February 1981.
6. Pauchard R., "Rayonnement d'une grille plane de fils continus et discontinus," Annales des Telecom., t 35 n° 9-10, pp 303-312, Sept. Oct. 1981.
7. Park, R., "Radant Lens: Alternative to Expensive Phased Arrays", *Microwave Journal*, Vol. 24, No. 9, pp 101-105, Sept. 1981. ■

Eigen Function Approach to a Class of Coupled Circular Cylindrical Rod Problems

S.H. Damle*, T.K. Seshadri*, K. Rajaiah**

Abstract

The problem of coupling between two circular cylindrical conductors located symmetrically along the normal distance between two parallel ground planes is analysed using an eigen function approach. Even and odd mode impedance values are presented for various parameters. Comparison of experimental results on a number of couplers as well as previously published results bear out the validity of the present results. New results for off-set slab line structure are also included.

Introduction

Cristal[1] has analyzed the problem of the coupled circular cylindrical rods, with the line joining their centres being parallel to the ground planes. However, another variant of the above structure which is more amenable to coupling variations is also possible by orienting the line joining the rod centres perpendicular to the ground plane. This type of structure does not seem to have been analyzed till now. In this paper an eigen function approach, which has been successfully utilized for the study of coaxial transmission line problems[2,3], will be used to analyze this structure.

Analysis

The geometry of the structure is shown in Figure 1(a), where D is the diameter of the rod and S and B are the separation between the centre of the circular rods and the ground planes respectively. The analysis consists in solving the odd and even mode excitations as Dirichlet and the mixed boundary value problems respectively satisfying the Laplace's equation in each case. The solution of Laplace's equation as applicable to the even and odd mode excitations of the coupling configuration is written in terms of the series of eigen functions such as

$$\phi = K + A_o \ln\left[\frac{r}{a}\right] + \sum_{m=1,2,3,\ldots} A_m (r^m - a^{2m} r^{-m}) \cos m\theta$$

where K is the potential on the centre conductor, A_o and A_m's are the unknown constants to be determined by the use of relevant boundary conditions and a is the radius of the circular centre conductor. The boundary conditions for the even and odd mode excitations are indicated in Figures 1(b) and 1(c).

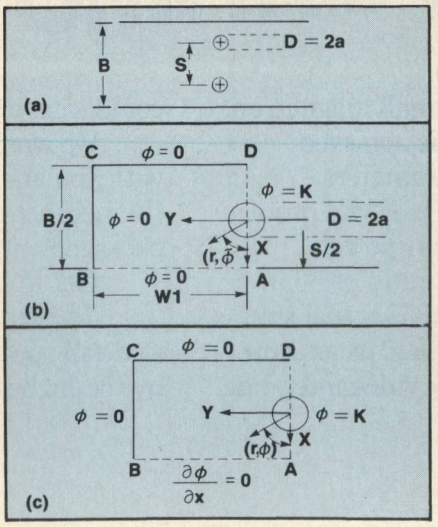

Fig. 1 (a) Geometry of the structure, (b) boundary conditions for odd mode excitations, (c) boundary conditions for even mode excitations.

The evaluation of the unknown constants is carried out by the use of the successive integration technique[4,5]. In this approach the error on the boundary is integrated successively and equated to zero. The residue identity equation is given by

$$\int_{S_1}^{S_2}\int_{S_1}^{S}\cdots\int_{S_1}^{S} R(dS)^{k+1} = \frac{1}{k!}\int_{S_1}^{S_2}(S_2 - S)^k\, R.dS.$$

where S^1, S^2 .... are the limits of the integral, R is the error and S is the running coordinate along the boundary edge. k = 0,1,2,.... denote the number of integrations. The above equation is used to generate a set of simultaneous equations corresponding to each boundary condition for the two modes of excitations. These are then solved by a suitable method to arrive at the constants. Once the potential functions are thus determined, the even and odd mode capacitances are determined in the usual way, leading finally to the even and odd mode impedance values.

Results and Discussions

Results of the calculations are shown in Figures 2 and 3, where Z_{oe} and Z_{oo} are plotted as functions of B/D and S/D. The special case of B/D = 2(S/D) in the case of odd mode excitation, corresponds to the standard symmetrical slab line configuration. Present results are tabulated along with those available in the literature[6] in Table 1. Comparison of the value shows an excellent agreement with the predicted results, the error being less than a percent. It may in fact be noted that the odd mode impedance

*Tata Institute of Fundamental Research, Bombay 400 005
**Indian Institute of Technology, Bombay 400 076

TABLE I

$\frac{B}{D}$	$\frac{B}{2D}$	SLAB LINE WHEELER[6] $Z_o \frac{B}{2D}$ ohms	PRESENT WORK $Z_{oo} \frac{S}{D} = \frac{B}{2D}$ ohms
10	5	110.7	111.1
8	4	97.5	97.8
6	3	80.2	80.5
5	2.5	69.2	69.6
4	2	55.7	56.1

data, as presented in Figure 3, can be used for obtaining the values of characteristic impedance of slab

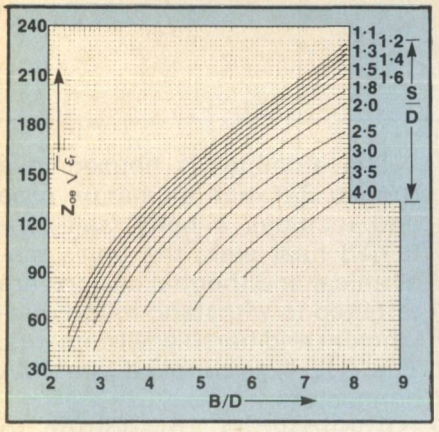

Fig. 2 Even mode impedance.

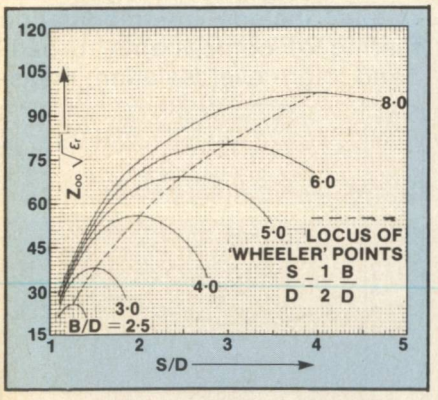

lines with off-centered circular inner conductor. This is considered as a new result not explicitly available in the literature.

The coupling configuration analysed above was used in the feeder system of a large UHF dipole array[7]. The experimental measurements on the couplers for this feeder system agree well with those predicted from the above analysis.

Conclusion

Eigen function approach has been successfully utilized for the solution of coupled rod transmission line problems with a rectangular outer boundary. Good agreement has been found between the theoretical and experimental results. New results on the characteristic impedance of an offset slab transmission line have also been presented.

The above method of analysis can also be extended to solve Cristal type filter structure and other coupled line configurations.

Acknowledgements

The authors would like to acknowledge the help of Prof. T.S. Saad during the course of this work. They are also thankful to Prof. R.V.S. Sitaram, Head, Microwave Division and Prof. B.V. Sreekantan, Director, T.I.F.R. for their kind encouragement.

REFERENCES

1. Cristal, E.G., 'Coupled circular cylindrical rods between parallel ground planes', IEEE Trans. vol. MTT-12, pp. 428-38, July 1964.
2. Seshadri, T.K., and K. Rajaiah, 'Accurate estimation of characteristics impedance of coaxial transmission line problems by eigen function approach', proc. IEEE, vol. 70, No. 1, pp. 82-84, January 1982.
3. Damle, S.H., T.K. Seshadri and K. Rajaiah, 'Eigen function approach to a class of coupled bar problems', proceedings of the International Symposium on Microwaves and Communications, pp. 69-72, Indian Institute of Technology, Kharagpur, India, December 1981.
4. Collatz, L., 'The numerical treatment of differential equations', Berlin, Germany, Springer Verlag, 1968.
5. Seshadri, T.K., et al., 'Corner function analysis of microstrip transmission lines', IEEE Trans. vol. MTT-28, pp. 376-380, April 1980.
6. Wheeler, H.A., 'The transmission line properties of a round wire between parallel planes', IRE Trans., Vol. AP-3, pp. 203-207, October 1955.
7. Kapahi, V.K., et al., 'An array of 968 dipoles for Ooty Radio Telescope', CSIR Symposium on Antennas, Indian Institute of Science, Bangalore, India, 1968. ■

1 Watt Amplifier Covers 700 MHz to 4200 GHz

Mini Circuit Lab.
Brooklyn, NY

As more systems and subsystems extend to 4 GHz and beyond, design engineers are experiencing a growing need for higher output than the milliwatt levels available from their signal/sweep generators and frequency synthesizers. Up to one-watt output is often necessary to perform adequate and meaningful testing of components and functional blocks. The model ZHL-42 wideband amplifier, with 1 watt output, provides the most economical solution to such requirements over the full 700 MHz to 4200 MHz band. It is shown in Fig. 1.

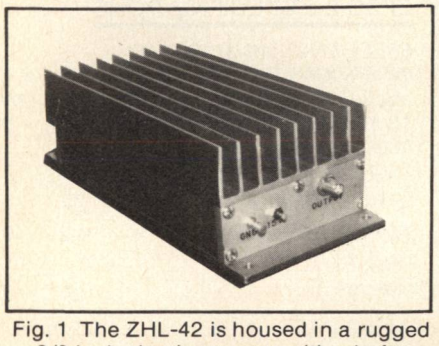

Fig. 1 The ZHL-42 is housed in a rugged 3/8 inch aluminum case with a hefty heat sink.

The four-stage, ultra-linear Class A amplifier provides 30 dB gain over the 700 to 4200 MHz frequency range, with gain flatness typically within 1.0 dB (see Figure 2). The ZHL-42 is unconditionally stable and can be connected to any load impedance without concern for amplifier damage or oscillation. Amplifier performance is summarized in Figures 3-5.

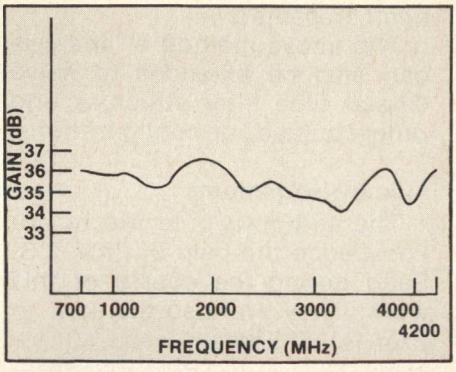

Fig. 2 Gain flatness, over the 700 to 4200 MHz range is typically 1.0 dB.

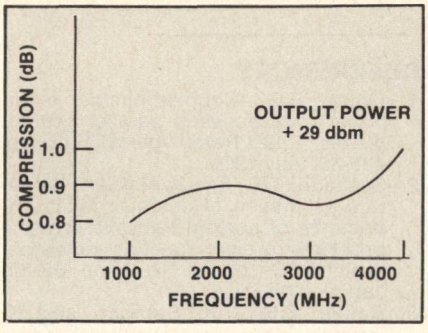

Fig. 3 Gain compression vs RF output level.

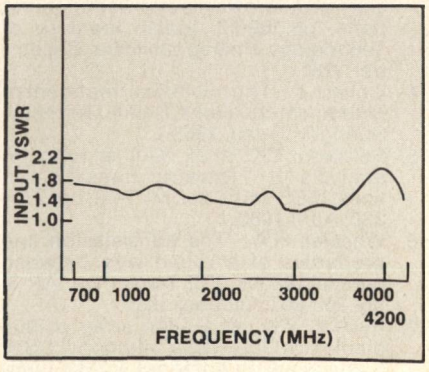

Fig. 4 Input VSWR vs frequency.

The amplifier is housed in a rugged 3/8 inch aluminum case and includes a hefty, self-contained heat sink; the unit's mechanical and thermal designs are targeted to withstand tough punishment and harsh environments. The ZHL-42 is supplied with SMA connectors.

Applications, in addition to boosting signal/sweep generator output, include intermodulation testing of components, broadband, high-level isolation, measurements and the achievement of linear gain in signal-processing systems.

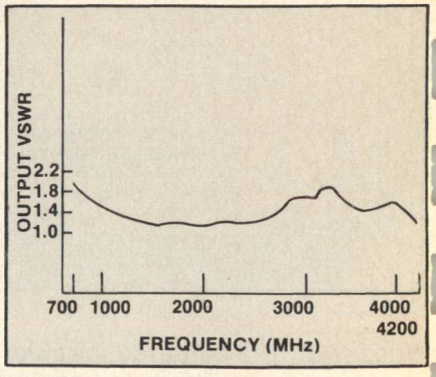

Fig. 5 Output VSWR vs frequency.

The ZHL-42 requires +15 volt DC, 0.69 A power supply input, operates over 0° to 65°C temperature range, and has a -55° to +100°C storage temperature range. Total allowable input RF power is +15 dBm with output loaded; +10 dBm when output is not loaded. Price: $895. Delivery: 1 week. R/S No. 244.

1982 EDITORIAL INDEX

COVERS

Avantek
"Integrated Marisat RF Up/Downlink Subsystem," No. 1, p. 98.

Aydin Microwave
"'Flatpack Amplifier," No. 7, p. 108.

California Eastern Labs
"Broadband Fixture Characterizes any Packaged Microwave Transistor," No. 10, p. 95.

Flann Microwave Instruments, Ltd.
"Microwave Network Analyzers for Millimetric Bands," No. 4, p. 89

Hewlett Packard
"Broadband Fixture Characterizes any Packaged Microwave Transistor," No. 10, p. 95.

M/A-COM
"Computer Aided Design and Manufacture of GaAs Hyperabrupt Varactors," No. 3, p. 99.

MA/-COM
"1nnkW Solid State L-Band Uplink Transmitter," No. 9, p. 158.

Marconi Instruments Ltd.
"Automatic Scalar Analyzer Uses Modern Technology," No. 4, p. 83.

Maury Microwave
"Broadband Fixture Characterizes any Packaged Microwave Transistor," No. 10, p. 95.

Mini Circuits
"1 watt 0.7-4.2 GHz Amplifier," No. 12, p. 136.

Raytheon
"The Cobra Judy Phased Array Radar," No. 2.

Scientific-Atlanta
"Millimeter-to-microwave converters," No. 6, p. 112.

Thomson-CSF
"3 kW 6 GHz Earth Station TWT Thomson-CSF DTE," No. 8, p. 114.

Watkins-Johnson
"Digitally Tuned PROM-Corrected VCO," No. 11, p. 131.

Wiltron
"Programmable Broadband Sweeper Delivers 40 mW Out From 2 to 18 GHz," No. 5, p. 164.

EDITORIALS

Topol, S.
"Satellite Communications — Still Emerging," No. 1, p. 16.

Sparks, R.
"Thirty Years of Microwaves," No. 5, p. 18.

TECHNICAL/APPLICATIONS SECTION

ANTENNAS

Bardash, Irwin
"Phased Arrays for ECM Applications," No. 9, p. 81.

Bhartia, P. and I. J. Bahl
"Frequency Agile Microstrip Antennas," No. 10, p. 68.

Collignon, G., Y. Michel, F. Robin, S. Saint, and J. C. Bolomey
"Quick Microwave Fields Mapping for Large Antennas," No. 12, p. 129.

Jamwal, K. K. S., A. Dhar and R. Vakil
"Analysis, Design and Characteristics of X-Band Dielectric Wedge Waveguide Antennas," No. 12, p. 99.

Maple, M. J., R. B. Wilds and J. K. Hunton
"Beam Forming Networks Using Composite Phase Shifters," No. 12, p. 79.

Starski, J. P., B. Ingemannsen and A. Olausson
"A Microprocessor Controlled Variable Phase and Amplitude Antenna Feed Network Unit," No. 10, p. 75.

Volta, P.
"Design and Development of an Omni Directional Antenna With a Collinear Array of Slots," No. 12, p. 111.

COMPONENTS/SUBSYSTEMS

Anzac Division, Adams-Russell
"Amplifier Applications Note," No. 10, p. 130.

Ayasli, Y.
"Microwave Switching with GaAs FETS," No. 11, p. 61.

Betaharon, K. and P. DeSantis
"Microwave Technology Development under INTELSAT R&D: A Review," No. 8, p. 43.

Blaine, C.
"Tunnel Diode Oscillators," No. 9, p. 156.

Brehm, G. E. and R. E. Lehmann
"Monolithic GaAs FET Low-Noise Amplifiers For X-Band Applications," No. 11, p. 103.

Budreau, A. J., A. J. Slobodnik and P. H. Carr
"Fast Frequency Hopping Achieved with SAW Synthesizers," No. 2, p. 71.

Coirault, R. and G. K. Smith
"Technologies for the Next European Satellites," No. 1, p. 83.

Degenford, J. E., R. G. Freitag, D. C. Boire and M. Cohn
"Broadband Monolithic MIC Power Amplifier Development," No. 3, p. 89.

Driver, M. C., G. W. Eldridge and J. E. Degenford
"Broadband Monolithic Integrated Power Amplifier in Gallium Arsenide," No. 11, p. 87.

Essen, Helmut
"Investigations on the Operating Modes of Millimeter Wave Gunn-Oscillators," No. 9, p. 150.

Forsythe, R. E.
"A Coherent, Solid State, 225 GHz Receiver," No. 7, p. 64.

Hartman, C. LS., R. J. Kansy, W. D. Daniels, and B. R. Potter
"SAW Devices for Military Communications, Radar, and EW Systems," No. 7, p. 73.

SPECIAL REPORTS

PRODUCT FEATURES

Advertising Index

*Euro Global Edition

Sales Representatives

Bernard Bossard Vice President **Howard Ellowitz** Publisher
Sandra Pasqualucci Mgr. Sales/Marketing Administration

NEW ENGLAND NEW YORK STATE, MID—ATLANTIC NORTHEAST-SOUTHEAST, AND MIDWEST
Ed Johnson
610 Washington Street
Dedham, MA 02026
Tel: (617) 326-8220
TWX: 710 348 0481

PACIFIC & MOUNTAIN TIME ZONES
David Heller
1000 Elwell Court
Suite 234
Palo Alto, CA 94303
Tel: (415) 969-3886

EUROPE
Bronwyn Holmes,
Derek Hopkins
25 Victoria Street
London SW1H OEX,
England
Tel: 44-(1)-222-0466
TLX: 851-8885744

JAPAN
Tokyo Representative Corporation
Yamaguchi Bldg.
2-12-9 Kanda Jimbocho
Chiyoda-ku,Tokyo 101 Japan
Tel: 230-4117,4118
Cable: REPRETIV Tokyo
TLX: J26860